

Experimental shape sensing of a wing structure using SSB-iFEM: Static assessment and dynamic wind tunnel test

Original

Experimental shape sensing of a wing structure using SSB-iFEM: Static assessment and dynamic wind tunnel test / Esposito, M., Sorrenti, M., Gherlone, M.. - In: MEASUREMENT. - ISSN 0263-2241. - ELETTRONICO. - 265:(2026). [10.1016/j.measurement.2026.120354]

Availability:

This version is available at: 11583/3006462 since: 2026-01-12T10:06:30Z

Publisher:

Elsevier

Published

DOI:10.1016/j.measurement.2026.120354

Terms of use:

This article is made available under terms and conditions as specified in the corresponding bibliographic description in the repository

Publisher copyright

(Article begins on next page)



Experimental shape sensing of a wing structure using SSB-iFEM: Static assessment and dynamic wind tunnel test

Marco Esposito¹*, Matteo Sorrenti¹, Marco Gherlone¹

Department of Mechanical and Aerospace Engineering, Politecnico di Torino, Corso Duca degli Abruzzi, 24, 10129 Torino, Italy

ARTICLE INFO

Keywords:

Structural Health Monitoring
iFEM
Shape sensing
Digital twin
Aerospace structures

ABSTRACT

Reconstructing the displacement field from discrete strain measurements, commonly known as shape sensing, plays a crucial role in the development of advanced Structural Health Monitoring (SHM) frameworks. Monitoring displacements throughout a structure's operational life provides valuable data for predictive maintenance strategies and supports the implementation of digital twin technologies. Among the various shape-sensing techniques, the inverse Finite Element Method (iFEM) has emerged as a prominent solution. However, despite its demonstrated effectiveness, the practical application of iFEM remains limited by the requirement for back-to-back strain sensor configurations, i.e., sensors installed on both surfaces of a thin-walled structure. To overcome this limitation, a new variant called Single Sensor Based iFEM (SSB-iFEM) has recently been proposed. In this work, SSB-iFEM is employed to perform, for the first time, shape sensing on an entire aerospace structure: the half-wing of a commercial hotliner. The test setup reflects the complexity and constraints of real industrial conditions, as only limited structural information is available due to the commercial nature of the test article. Furthermore, the structure is instrumented exclusively on the accessible external surface and tested under simulated operating conditions in a wind tunnel. The experimental results demonstrate the high versatility and accuracy of SSB-iFEM, even when using a reduced set of strain sensors. This study proves that the proposed formulation successfully overcomes the main limitations of standard iFEM and significantly extends the applicability of shape sensing approaches to real-world aerospace structures.

1. Introduction

Aircraft, civil, and marine structural systems are susceptible to progressive structural degradation, often demanding complex and high-cost maintenance interventions. To address these challenges, Structural Health Monitoring (SHM) technologies are evolving rapidly, offering valuable insights to enhance structural safety while lowering maintenance costs [1]. Among the various SHM strategies, shape-sensing techniques, based on reconstructing the structural displacement field from discrete strain measurements, have experienced growing success. These methods provide evaluations of displacement, strain, and stress fields, enabling early detection of damage [2,3], assessment of remaining service life, and integration with control systems for morphing structures [4,5]. Their ability to operate in real time also aligns them closely with the structural digital twin concept.

Several shape-sensing methodologies exist in the open literature. Although they rely on the same type of input, strain data from a limited set of sensors, they differ in their underlying computational frameworks [6].

A class of these methods employs predefined basis functions, with unknown coefficients adjusted to best fit the measured strains. The Modal Method (MM), for example, represents structural deformation using mode shapes as basis functions [7,8], which are typically derived from experimental results or numerical models. Since generating these mode shapes can be resource-intensive, selection strategies based on energy contribution are commonly applied to reduce the considered modes, by selecting those that contribute the most to the target deformed shape [9]. Strategic placement of sensors has been shown to enhance performance even when only a few are used [10], and recent advancements have extended such techniques to highly flexible wings undergoing significant deflections [11].

Another major category consists of strain-integration approaches, particularly suited for slender structures. These methods often assume classical beam theory and derive deflections from measured axial strains. Ko's Displacement Theory stands out in this group. Introduced in [12], it reconstructs beam deflections by integrating axial strains twice, using measurements collected along a known sensing line, offset from the neutral axis by a known quantity. In addition to simple

* Corresponding author.

E-mail address: marco.esposito@polito.it (M. Esposito).

bending, torsional effects can also be captured, either by orienting strain sensors along a 45° direction path or by implementing a double-line sensor setup. This theory has been successfully applied to a finite element model of the Ikhana UAV's doubly tapered wing [13] and has undergone experimental validation [14]. Additional applications include shape monitoring of a vertical take-off and landing (VTOL) UAV [15], cantilevered swept wings [16], and composite laminates such as CFRP [17].

In order to enhance shape-sensing methodologies with the potentialities of Physics Informed Machine Learning (PIML) [18], a recent attempt has been presented in [19], where an inverse Physics Informed Neural Network (iPINN) is developed for displacement reconstruction. The iPINN was trained on direct problem datasets, and its performance was compared with the MM approach. The results, although promising, demonstrated a strong sensitivity of the iPINN on the selected sensor configuration.

More recently, a method based on discretising the structural domain with finite elements has gained attention for its flexibility and robustness in shape sensing, the inverse Finite Element Method (iFEM). Initially introduced in [20], iFEM reconstructs displacement fields by expressing strains as derivatives of shape functions multiplied by the unknown nodal degrees of freedom (DOFs). The unknowns are computed by minimising a weighted-least-squares error functional that quantifies the discrepancy between measured and reconstructed strains. The error functional is computed for membrane and bending strain measures, which can be easily computed from sensors installed in a back-to-back configuration for a thin-walled structure. Crucially, iFEM depends only on kinematic relationships, without requiring knowledge of material properties or loading conditions. The method was first applied to thin-shell structures using a triangular three-node element (iMIN3) [20], and later extended to four-node quadrilaterals (iQS4) [21], curved eight-node elements [22], and isogeometric elements [23,24]. Developments have also included nonlinear extensions for large deformation analysis [25,26], as well as specialised versions for layered composites and sandwich panels with highly heterogeneous stacking sequences [27–29]. Additionally, one-dimensional inverse elements grounded in Timoshenko beam theory have been developed for truss and beam applications [30], including variants for structures with nonuniform or complex cross-sections [31,32]. Hybrid iFEM schemes, which integrate both one- and two-dimensional inverse elements, have proven effective in the analysis of stiffened panels and similar structural systems [33].

Comparative studies in the literature [6,34–36] indicate that MM and iFEM are among the most versatile and effective shape-sensing techniques for general and complex structures. In particular, iFEM has the potential to offer higher accuracy even in the presence of uncertainties, although this comes at the cost of requiring a large number of strain measurements and corresponding sensors [34,35]. To address this limitation, various strategies have been explored. For example, sensor placement optimisation has been investigated to enhance the accuracy of displacement field reconstruction for a limited number of sensors [34,37]. Another promising approach is to pre-extrapolate the strain field before using it as input to iFEM [38–42].

The inverse Finite Element Method has demonstrated broad applicability across various engineering domains, including marine [43–45] and civil structures [46,47]. In the aerospace sector, iFEM applications have primarily focused on component-level analyses, such as aerospace panels [48,49], wing-shaped sandwich structures [39], and CFRP-stiffened plates [33]. To date, only one study in the open literature has addressed the application of iFEM to a full wing structure [50], though that investigation was limited to numerical simulations. The main obstacle hindering the experimental application of iFEM to complex structures lies in its requirement for back-to-back sensor placement. The conventional iFEM formulation relies on the evaluation of both membrane and bending strain measures, which necessitates strain measurements on both the inner and outer surfaces

of thin-walled structures. In experimental scenarios, however, access to both surfaces of components such as wings is often not feasible, making the installation of such sensor configurations impractical. To address this limitation, a multilayer perceptron (PMLP) neural network was proposed in [51] to reconstruct strain data on both surfaces of a plate using only single-sided strain measurements. Though promising, this approach increases the complexity of the procedure by requiring prior training of the neural network. Moreover, the approach was validated for only a single load case, without demonstrating generalisation to different loading conditions. A more comprehensive and straightforward solution to this challenge was recently introduced in [52], where the Single Sensor Based inverse Finite Element Method (SSB-iFEM) was presented. The method modifies the standard iFEM weighted-least-squares error functional by directly incorporating the sensor strain measurements and comparing them with the corresponding analytical strain values. By formulating the problem in terms of actual sensor data rather than derived strain measures (membrane strains and bending curvatures), this approach removes the need for back-to-back sensor placement and enables the use of single-sided sensor configurations.

This work presents the first experimental application of the Single Sensor Based inverse Finite Element Method (SSB-iFEM), and more broadly, of iFEM-based approaches, for the structural monitoring of a full half-wing under dynamic aerodynamic loads. The structure under investigation is the half-wing of a commercial hotliner, experimentally tested using strain sensors placed solely on the external, and only accessible, surface. The half-wing first undergoes a static experiment on a test bench, and is subsequently subjected to experimentally simulated operating conditions in a wind tunnel. These tests are particularly significant, as limited information about the structure is available due to its commercial origin. As such, the study highlights a key advantage of the iFEM-based approaches with respect to other shape-sensing techniques: they require only geometric data and can be applied even when material properties are unknown. Furthermore, the methods are capable of reconstructing the full deformed shape of the structure and, in some cases, even of components with unknown geometrical characteristics. In the study, the SSB-iFEM is benchmarked against the standard iFEM. To enable this comparison, it is assumed that the standard iFEM operates under the hypothesis of a constant through-the-thickness strain distribution. The results show that while SSB-iFEM accurately reconstructs the deformed shape of the half-wing, the standard iFEM yields significantly inaccurate results. This confirms that SSB-iFEM is the only practical solution for complex aerospace structures with limited access to a single surface. Moreover, even in cases where both surfaces are accessible, SSB-iFEM still offers the advantage of reducing the number of required sensors. Finally, the wind tunnel test demonstrates that the SSB-iFEM is capable of performing real-time monitoring of an aerospace structure under dynamic operating conditions with high accuracy, thereby enabling the realisation of a structural digital twin.

The paper is structured as follows. In Section 2, standard iFEM and SSB-iFEM are introduced. The half-wing and the static assessment configuration and results are described in detail in Section 3. In Section 4, the results of the wind tunnel experimental analysis are reported and discussed. Finally, in Section 5, the concluding remarks are formulated.

2. Inverse Finite Element Method: original and SSB formulations

This section summarises both existing inverse Finite Element formulations for thin-walled structures, the original one developed by Tessler et al. [20], henceafter simply denoted as iFEM, and the recently proposed SSB-iFEM, [52].

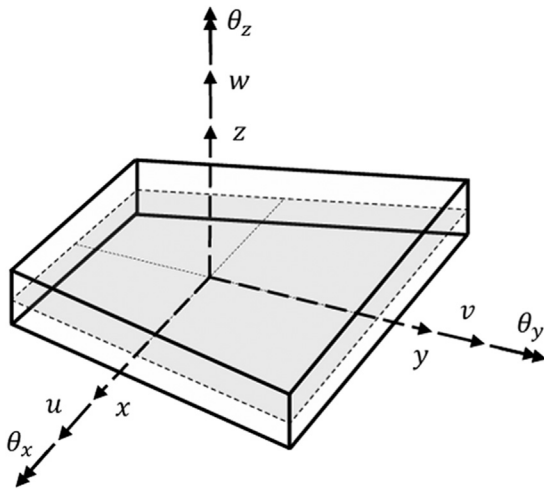


Fig. 1. Kinematic variables of FSDT [33].

2.1. Kinematic assumptions and finite element approximation

Both iFEM and SSB-iFEM for plate and shell structures are based on the kinematic assumptions of the First-order Shear Deformation Theory (FSDT). Let us consider a plate with total thickness $2t$, referred to a Cartesian reference system, with z being the thickness coordinate ranging between $z = -t$ and $z = +t$ and the plate mid-surface belonging to the (x, y) plane, Fig. 1. According to FSDT, the displacement components u_x , u_y , and u_z can be written as follows

$$\begin{aligned} u_x(x, y, z) &= u(x, y) + z\theta_y(x, y) \\ u_y(x, y, z) &= v(x, y) - z\theta_x(x, y) \\ u_z(x, y, z) &= w(x, y) \end{aligned} \quad (1)$$

where the kinematic variables $\mathbf{u} = \{u, v, w, \theta_x, \theta_y\}^T$ are: u and v (mid-surface displacements in the x and y directions, respectively), w (transverse deflection), θ_x and θ_y (rotations about the x - and y -axis, respectively), Fig. 1.

Using the linear strain–displacement relations yields the strain field

$$\begin{aligned} \boldsymbol{\epsilon}_p &= \begin{Bmatrix} \epsilon_{xx} \\ \epsilon_{yy} \\ \gamma_{xy} \end{Bmatrix} = \begin{Bmatrix} u_{,x} \\ v_{,y} \\ u_{,y} + v_{,x} \end{Bmatrix} + z \begin{Bmatrix} \theta_{y,x} \\ -\theta_{x,y} \\ \theta_{y,y} - \theta_{x,x} \end{Bmatrix} = \mathbf{m}(\mathbf{u}) + z\mathbf{k}(\mathbf{u}) \\ &= \mathbf{Z}_{\epsilon_p}(z) \begin{Bmatrix} \mathbf{m}(\mathbf{u}) \\ \mathbf{k}(\mathbf{u}) \end{Bmatrix} \end{aligned} \quad (2)$$

$$\boldsymbol{\gamma}_s = \begin{Bmatrix} \gamma_{xz} \\ \gamma_{yz} \end{Bmatrix} = \begin{Bmatrix} w_{,x} + \theta_y \\ w_{,y} - \theta_x \end{Bmatrix} = \mathbf{g}(\mathbf{u}) \quad (3)$$

with $\mathbf{Z}_{\epsilon_p}(z) = [\mathbf{I} \quad z\mathbf{I}]$. The *in-plane strains* $\boldsymbol{\epsilon}_p$ are expressed in terms of *in-plane strain measures* \mathbf{m} and \mathbf{k} (membrane strains and bending curvatures, respectively), and the *transverse shear strains* $\boldsymbol{\gamma}_s$ correspond to the *transverse shear strain measures*, \mathbf{g} .

As for the direct FEM, in both the iFEM and SSB-iFEM the structure is discretised into finite elements. Within each element, the kinematic variables \mathbf{u} are expressed in terms of the nodal degrees of freedom (DOFs) of the element, \mathbf{u}^e , through the shape functions \mathbf{N}

$$\mathbf{u} = \mathbf{N}\mathbf{u}^e \quad (4)$$

The strain field defined by Eqs. (2) and (3) is consequently approximated as

$$\boldsymbol{\epsilon}_p = \mathbf{m}(\mathbf{u}^e) + z\mathbf{k}(\mathbf{u}^e) = \mathbf{B}^m\mathbf{u}^e + z\mathbf{B}^k\mathbf{u}^e = \mathbf{Z}_{\epsilon_p}(z) \begin{Bmatrix} \mathbf{B}^m \\ \mathbf{B}^k \end{Bmatrix} \mathbf{u}^e = \mathbf{Z}_{\epsilon_p}(z)\mathbf{B}^{mk}\mathbf{u}^e \quad (5)$$

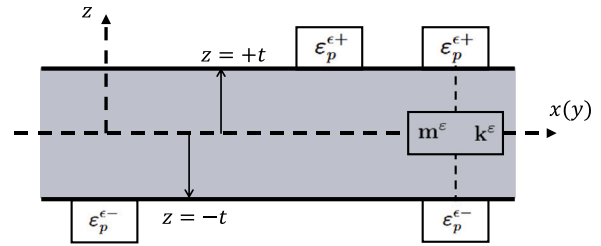


Fig. 2. Strain sensors on top and/or bottom surface of a thin-walled structure. Experimental in-plane strain measures (\mathbf{m}^ϵ and \mathbf{k}^ϵ) are available only where back-to-back sensors are used.

$$\boldsymbol{\gamma}_s = \mathbf{g}(\mathbf{u}^e) = \mathbf{B}^g\mathbf{u}^e \quad (6)$$

where \mathbf{B}^m , \mathbf{B}^k , \mathbf{B}^{mk} and \mathbf{B}^g are matrices of shape functions derivatives. In particular, the iQS4-inverse quadrilateral element is here considered and the detailed expressions of the shape functions and corresponding derivatives can be found in [21].

2.2. Experimental strain measurements and strain measures

Shape sensing is based on the availability of a discrete number of strain sensors able to provide the corresponding *strain measurements*. Considering strain sensors (linear strain gauges, rosettes, or fibre optical sensors) attached on the top ($z = +t$) and/or bottom ($z = -t$) surface of the thin-walled structure (Fig. 2), the corresponding *in-plane strain measurements*, are, respectively,

$$\boldsymbol{\epsilon}_p^{\epsilon+} = \begin{Bmatrix} \epsilon_{xx}^{\epsilon+} \\ \epsilon_{yy}^{\epsilon+} \\ \gamma_{xy}^{\epsilon+} \end{Bmatrix}, \quad \boldsymbol{\epsilon}_p^{\epsilon-} = \begin{Bmatrix} \epsilon_{xx}^{\epsilon-} \\ \epsilon_{yy}^{\epsilon-} \\ \gamma_{xy}^{\epsilon-} \end{Bmatrix} \quad (7)$$

where the super-script ϵ denotes the experimental origin of the quantity. If sensors are arranged in a back-to-back configuration, Fig. 2, the corresponding *experimental in-plane strain measures*, \mathbf{m}^ϵ and \mathbf{k}^ϵ , can be easily evaluated as

$$\mathbf{m}^\epsilon = \frac{1}{2}(\boldsymbol{\epsilon}_p^{\epsilon+} + \boldsymbol{\epsilon}_p^{\epsilon-}), \quad \mathbf{k}^\epsilon = \frac{1}{2t}(\boldsymbol{\epsilon}_p^{\epsilon+} - \boldsymbol{\epsilon}_p^{\epsilon-}) \quad (8)$$

Since the experimental measurement of the transverse shear strains is not possible, the *experimental transverse shear strain measures*, \mathbf{g}^ϵ , are always unavailable.

2.3. iFEM error functional

The iFEM error functional is based on a least-square error between the analytical strain measures (\mathbf{m} , \mathbf{k} , \mathbf{g}) and the experimental strain measures (\mathbf{m}^ϵ , \mathbf{k}^ϵ , \mathbf{g}^ϵ). At the element level, the error is defined as

$$\Phi^e(\mathbf{u}^e) = \boldsymbol{\lambda}_m \cdot \Phi_m(\mathbf{u}^e) + \boldsymbol{\lambda}_k \cdot \Phi_k(\mathbf{u}^e) + \boldsymbol{\lambda}_g \cdot \Phi_g(\mathbf{u}^e) \quad (9)$$

where $\boldsymbol{\lambda}_m$, $\boldsymbol{\lambda}_k$, and $\boldsymbol{\lambda}_g$ are the vectors of penalisation factors and Φ_m , Φ_k , and Φ_g are the vectors of individual error functionals corresponding to the membrane, curvature and transverse shear strain measures, respectively,

$$\Phi_m = \int_{A^e} [\mathbf{m}(\mathbf{u}^e) - \mathbf{m}^\epsilon]^2 dA^e \quad (10)$$

$$\Phi_k = (2t)^2 \int_{A^e} [\mathbf{k}(\mathbf{u}^e) - \mathbf{k}^\epsilon]^2 dA^e \quad (11)$$

$$\Phi_g = \int_{A^e} [\mathbf{g}(\mathbf{u}^e) - \mathbf{g}^\epsilon]^2 dA^e \quad (12)$$

where A^e is the area of the element and the operator $(\cdot)^2$ represents the Hadamard power.

The penalisation factors $\boldsymbol{\lambda}_m$, $\boldsymbol{\lambda}_k$, and $\boldsymbol{\lambda}_g$ control the degree of compatibility enforced between the analytical and experimental strain measures. These factors are also used to deal with the unavailability of

experimental strain measures within the element, in particular by setting a penalisation factor to 1 or to a small value (for example, 10^{-5}) if the corresponding experimental strain measure is available or not, respectively. Since transverse shear strain measures \mathbf{g}^e cannot be evaluated experimentally, they are assumed to be $\mathbf{0}$, thus leading to a simplified definition of the related least-square error

$$\Phi_g = \int_{A^e} \mathbf{g}(\mathbf{u}^e)^{\circ 2} dA^e \quad (13)$$

and requiring small values of the corresponding penalisation factors, $\lambda_g = \{10^{-5}, 10^{-5}\}$. Considering that the experimental evaluation of the in-plane strain measures requires back-to-back sensors, Eq. (8), $\lambda_m = \lambda_k$ and the following cases are possible: tri-axial strain rosettes $\lambda_m = \lambda_k = \{1, 1, 1\}$, no strain sensors at all $\lambda_m = \lambda_k = \{10^{-5}, 10^{-5}, 10^{-5}\}$, linear strain-gauges along the x -axis $\lambda_m = \lambda_k = \{1, 10^{-5}, 10^{-5}\}$ (and values modified accordingly if linear strain-gauges are measuring only in the y -direction or if the in-plane shear strain γ_{xy} is only measured).

Substituting Eqs. (5) and (6) into Eqs. (10), (11), and (13) and these into the definition of the element error functional, Eq. (9), and then minimising with respect to the element nodal DOFs \mathbf{u}^e , yields the element-level system of linear algebraic equations

$$\frac{\partial \Phi^e(\mathbf{u}^e)}{\partial \mathbf{u}^e} = \mathbf{K}^e \mathbf{u}^e - \mathbf{f}^e = 0 \implies \mathbf{K}^e \mathbf{u}^e = \mathbf{f}^e \quad (14)$$

The definition of \mathbf{K}^e and \mathbf{f}^e is reported in Appendix A. Transforming from the local-element to the global-structure coordinate system and assembling the contributions of the whole set of inverse elements, lead to the global-structure system of algebraic equations

$$\mathbf{K}\mathbf{U} = \mathbf{F} \quad (15)$$

where \mathbf{U} contains the nodal DOFs of the discretised structure, the global matrix \mathbf{K} depends on the sensors location only, whereas the global vector \mathbf{F} depends on both the sensors location and on the experimental strain measures. The solution of (15), upon prescribing the proper geometric boundary conditions, is efficient since it involves inverting \mathbf{K} only once even when a dynamic problem is considered with time-varying \mathbf{F} [20].

2.4. SSB-iFEM error functional

Since the requirement for back-to-back sensors of iFEM can be difficult, if not impossible, to meet in several applications, the SSB-iFEM formulation has been introduced in order to overcome this drawback. The SSB-iFEM error functional is in fact defined as the least-square error between the analytical strains and the corresponding experimental strain measurements available on the top and/or bottom surface of the thin-walled structure. For a single inverse element, the error is expressed as

$$\Psi^e(\mathbf{u}^e) = \lambda_p^+ \cdot \Psi_p^+(\mathbf{u}^e) + \lambda_p^- \cdot \Psi_p^-(\mathbf{u}^e) + \lambda_g \cdot \Psi_g(\mathbf{u}^e) \quad (16)$$

As for the iFEM formulation, λ_p^+ , λ_p^- , and λ_g are the vectors of penalisation factors and Ψ_p^+ , Ψ_p^- , and Ψ_g are the vectors of individual error functionals whose definition is

$$\Psi_p^+ = \int_{A^e} [\boldsymbol{\epsilon}_p(+t, \mathbf{u}^e) - \boldsymbol{\epsilon}_p^{e+}]^{\circ 2} dA^e \quad (17)$$

$$\Psi_p^- = \int_{A^e} [\boldsymbol{\epsilon}_p(-t, \mathbf{u}^e) - \boldsymbol{\epsilon}_p^{e-}]^{\circ 2} dA^e \quad (18)$$

$$\Psi_g = \int_{A^e} \boldsymbol{\gamma}_s(\mathbf{u}^e)^{\circ 2} dA^e = \int_{A^e} \mathbf{g}(\mathbf{u}^e)^{\circ 2} dA^e = \Phi_g \quad (19)$$

The role of the penalisation factors λ_p^+ , λ_p^- , and λ_g is similar to that already described for iFEM. Moreover, these coefficients also accompany the increased flexibility of SSB-iFEM with respect to iFEM in terms of strain sensor configuration. Since a back-to-back arrangement is not required, λ_p^+ and λ_p^- need not to coincide. For example, if a linear strain gauge in the y -direction is available on the bottom surface only, $\lambda_p^+ = \{10^{-5}, 10^{-5}, 10^{-5}\}$ and $\lambda_p^- = \{10^{-5}, 1, 10^{-5}\}$. As expressed by Eq. (19), the

individual error functional $\Psi_g = \Phi_g$ represents a common term between iFEM and SSB-iFEM and the same penalisation strategy holds for the definition of λ_g . The SSB-iFEM formulation clearly includes the iFEM one as a particular case (although with slight differences, refer to [52] for further details) when back-to-back sensors are considered.

Eqs. (5) and (6) are introduced into Eqs. (17)–(19), and the latter are further substituted into Eq. (16), thus leading to an expression of the SSB-iFEM error functional depending on the nodal DOFs \mathbf{u}^e . Minimisation with respect to \mathbf{u}^e provides the inverse element-level system of algebraic equations

$$\frac{\partial \Psi^e(\mathbf{u}^e)}{\partial \mathbf{u}^e} = \mathbf{K}'^e \mathbf{u}^e - \mathbf{f}'^e = 0 \implies \mathbf{K}'^e \mathbf{u}^e = \mathbf{f}'^e \quad (20)$$

The definition of \mathbf{K}'^e and \mathbf{f}'^e is reported in Appendix A. The usual straightforward treatment of (20), including local-to-global coordinate system transformation and assembly, leads to the global-structure matrix equation

$$\mathbf{K}'\mathbf{U} = \mathbf{F}' \quad (21)$$

where \mathbf{K}' and vector \mathbf{F}' have properties and roles similar to those of \mathbf{K} and \mathbf{F} , respectively.

In the context of this work, both the iFEM and SSB-iFEM formulations are implemented in the in-house DIMOSS[®] (Displacement Monitoring using Strain Sensors) software [53] (<https://dimoss.net/>). This is a MATLAB/Python-based code for SHM entirely developed within the AESDO (Aircraft and Engine Structural Design and Optimisation) research group of Politecnico di Torino.

3. Static assessment

This section presents the static experimental setup adopted to assess and compare the accuracy and robustness of the recently formulated SSB-iFEM and of the original iFEM. Furthermore, the inverse FE model and sensor configuration are described and discussed in detail.

3.1. Half-wing structure

The structure considered in this experimental campaign is a commercial hotliner produced by the Robbe modelsport company. Specifically, the selected model is the ‘‘Limit PRO’’ hotliner, with a Glass-Fibre-Reinforced-Polymer/Carbon-Fibre-Reinforced-Polymer (GFRP/CFRP) structure. The full aircraft consists of a wing (aspect ratio 12.3, airfoil MH-30), fuselage, and horizontal tail. For the purposes of this study, only the wing component is considered (see Fig. 3), and, taking advantage of the symmetry of the structure and of the loading condition, only half-wing is analysed.

This wing is particularly significant for different reasons. Firstly, it is the first commercial product experimentally monitored using iFEM (or SSB-iFEM). Secondly, its structural configuration can also represent larger-scale aircraft, such as gliders and ultralight aircraft. Thirdly, the geometrical and material characteristics are not fully known. In fact, the manufacturer has not provided any details on the material properties and wing geometry, apart from overall dimensions and airfoil data. However, upon this last aspect, one major advantage of the iFEM approach, compared to the traditional direct FEM or other existing shape-sensing techniques, is that material properties are not required to perform the analysis. Moreover, although iFEM requires an accurate geometric description of the structure in order to generate the inverse mesh and to correctly locate the strain sensors, it is possible to exclude components or parts from the inverse model. This can apply to components whose displacement field is not important to reconstruct or that cannot be instrumented with strain sensors. While this might appear to be an approximation, it is not, since the inverse model is fed with strain data that are inherently influenced by structural components, including those that are not present in the model.



Fig. 3. Wing.

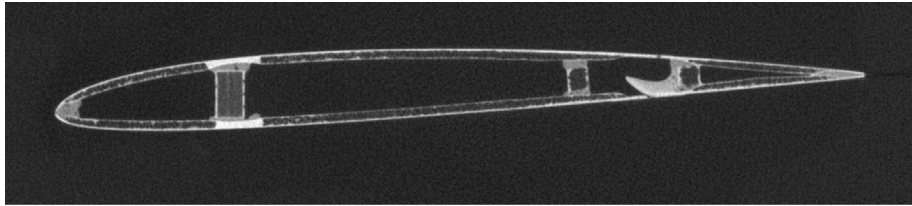


Fig. 4. CT scan of a cross-section close to the wing's tip, in the aileron region.

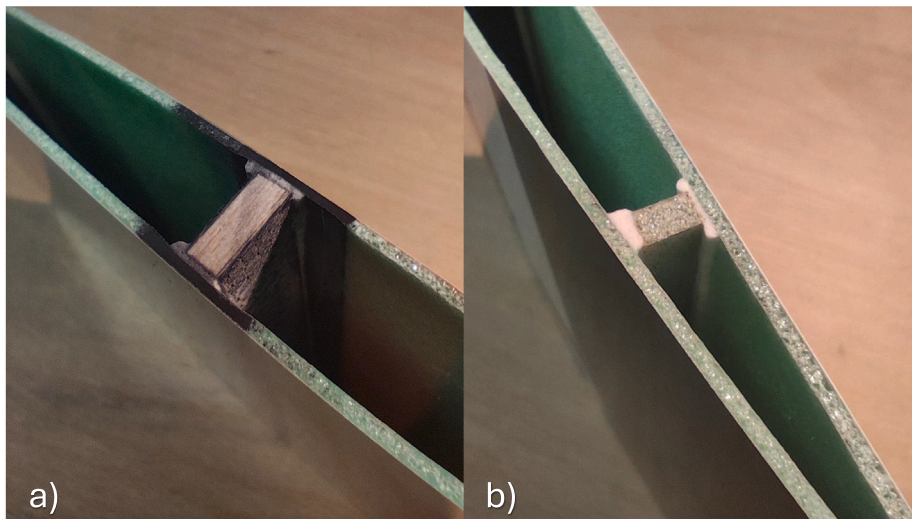


Fig. 5. Details of the wing inner structure: (a) front spar; (b) rear spar.

Since the wing cannot be disassembled, a reverse engineering process is required to retrieve the necessary geometrical features. Thus, a second wing, identical to the first one, was purchased and cut into different segments along its wingspan direction. Subsequently, each part was scanned using Computed Tomography (CT) to obtain the cross-sectional geometry. The CT scans were performed at the J-TECH (Advanced Joining Technologies) laboratory at Politecnico di Torino. Fig. 4 reports, as an example, a cross-section close to the wing's tip, in the aileron region.

The CT scans and the cut specimens revealed that the wing structure consists of a skin and of two main spars of different lengths. The skin, with a constant thickness $2t = 1.45$ mm, is made of a lightweight foam reinforced with GFRP. The front spar, which is the shortest one, is made of balsa wood covered by a thin layer of CFRP, as shown in Fig. 5(a). The rear spar, i.e., the longest one, is made of the same material used for the skin, see Fig. 5(b). Taking advantage of the iFEM feature previously discussed, given that it is impossible to set strain sensors inside the wing box, both spars are excluded from the reconstructed geometry and, therefore, not represented in the inverse model.

As shown in Fig. 6, a hole is present on the lower wing skin surface to locate the servos. Although it presents a complex geometry, it can be modelled in a simplified manner, that is, as a rectangular hole (see Fig. 6).

The spatial resolution of CT cross-section scans is lower than 0.15 mm; however, to reconstruct a smoother geometrical model, only a

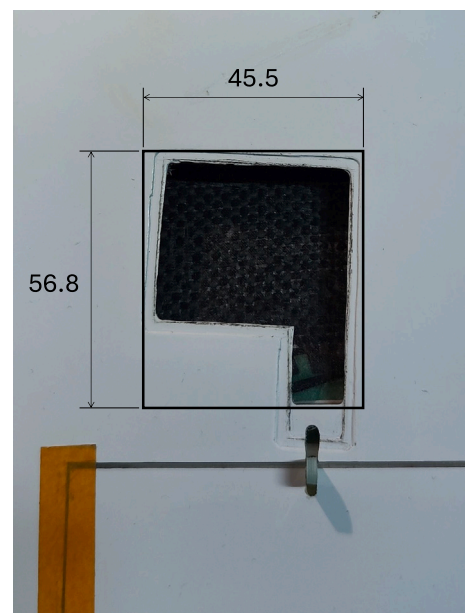


Fig. 6. Servos hole and dimensions (in mm).

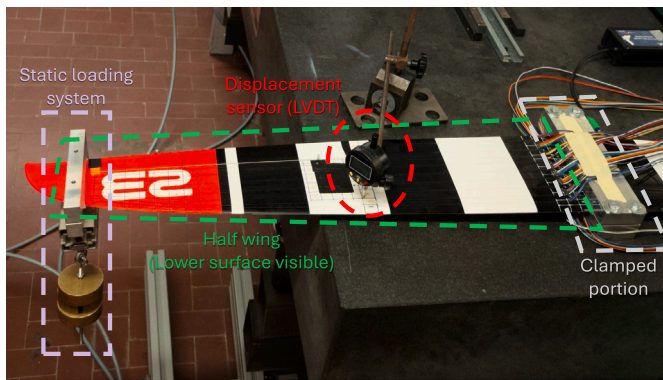


Fig. 7. Static experimental setup: half wing, loading and constraint systems.

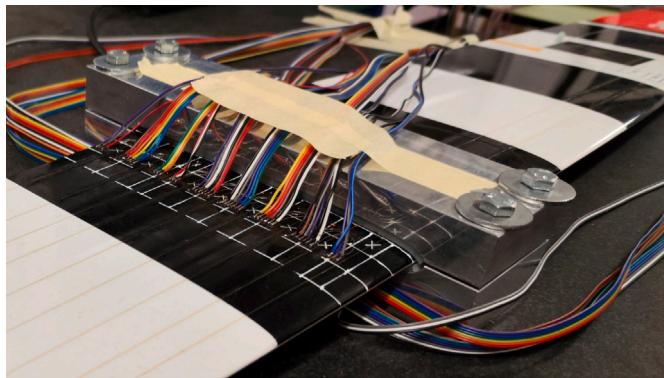


Fig. 8. Clamped portion: aluminium blocks and silicone sheets.

limited number of images were considered. The selected CT scan images were imported into SOLIDWORKS® and used to create the reference geometry. More specifically, the MH-30 airfoil profile was adapted to reconstruct the middle line of the skin profile and, subsequently, used to generate the reference surface of the wing structure through a sweep function along the wingspan direction.

The obtained geometry is then imported into MSC PATRAN© as a surface feature. However, before generating the mesh, three geometry edits are required. First, the servo hole is created according to the dimension reported in Fig. 6. Second, the aileron is removed from the geometry since it is considered not to contribute to the wing stiffness. Third, the wing tip beyond the loaded section (See Fig. 7) is also removed as strains are expected to be null and, for this reason, no strain sensors have been installed and no inverse elements are required.

The wing is tested in a cantilever configuration subjected to a concentrated transverse force near the wing tip, as shown in the scheme of Fig. 7. The clamped condition is recreated using two aluminium blocks that lock the wing and fix it to the testing table. Two thin silicone sheets have been placed between the wing and the blocks to ensure a better fit and prevent damage to the structure (see Section 3.3). Fig. 8 shows the clamped portion of the wing structure. The loading system that generates a concentrated force consists of two aluminium blocks hooking the wing section. Similarly to the clamped section, two thin silicone sheets are added around the wing surface to accommodate the wing profile without damaging the structure. The lower block is connected to an aluminium profile that holds the weights as shown in Fig. 9.

The structure is mounted upside down, so that the application of the weights generates a load that is in the same direction as the aerodynamic lift under operational conditions. An identical loading system to that shown in Fig. 9 is placed at the opposite end of the other half-wing in order to re-create a symmetric loading condition. Although

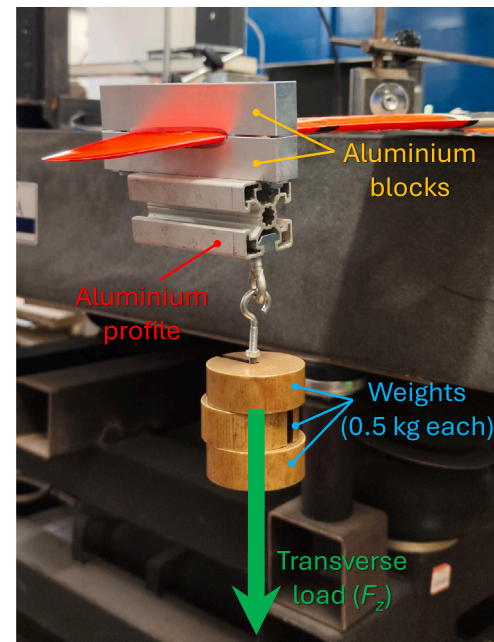


Fig. 9. Loading system and its main components.

not necessary for the iFEM analysis, for the sake of completeness, the location of the applied load is reported in Fig. 10.

3.2. Inverse FE model

This section presents the details of the inverse model used to assess the SSB-iFEM formulation implemented in DIMOSS® software and to compare its performance with that of the original iFEM.

Taking advantage of the symmetry of the wing's structure, loading and clamped conditions, only half of the wing is considered for the digital model. The inverse FE model of the half wing consists of 941 iSQ4 elements and 994 nodes, as shown in Fig. 10. As previously explained, both spars, the aileron and the wing tip are not included in the model.

Although the aluminium blocks aim to recreate the fully clamped condition by limiting displacements and rotations of the wing root section, as shown in Fig. 10, these may not be completely suppressed. In fact, the wing box, being hollow, allows some deformation, and the presence of the silicone sheets does not ensure a zero-displacement condition. According to the real loading configuration, the half-wing is constrained by applying a symmetry condition to the nodes belonging to the wing's mid-section ($x = 0$ in Fig. 10). More specifically, the constrained degrees of freedom for symmetry conditions are one displacement, i.e., $u = 0$, and two rotations, i.e., $\theta_y = \theta_z = 0$. Additionally, the half-wing is bolted to the upper aluminium block at two points, physically restricting displacements, i.e., $u = v = w = 0$ at the corresponding bolt nodes in the inverse FE model (refer to Fig. 10).

3.3. Sensor configuration

The half-wing is instrumented with strain sensors, which provide inputs for the shape-sensing process, and with displacement sensors, which provide feedback values for the evaluation of the accuracy of the displacement reconstruction.

Two kinds of strain sensors are installed on the structure: strain rosettes and fibre optic sensors. As already highlighted, the half-wing is designed so that the internal wing box is inaccessible and cannot be sensorised. Therefore, strain sensors can only be applied on the skin's external surface, leaving the internal one and the spars lacking any

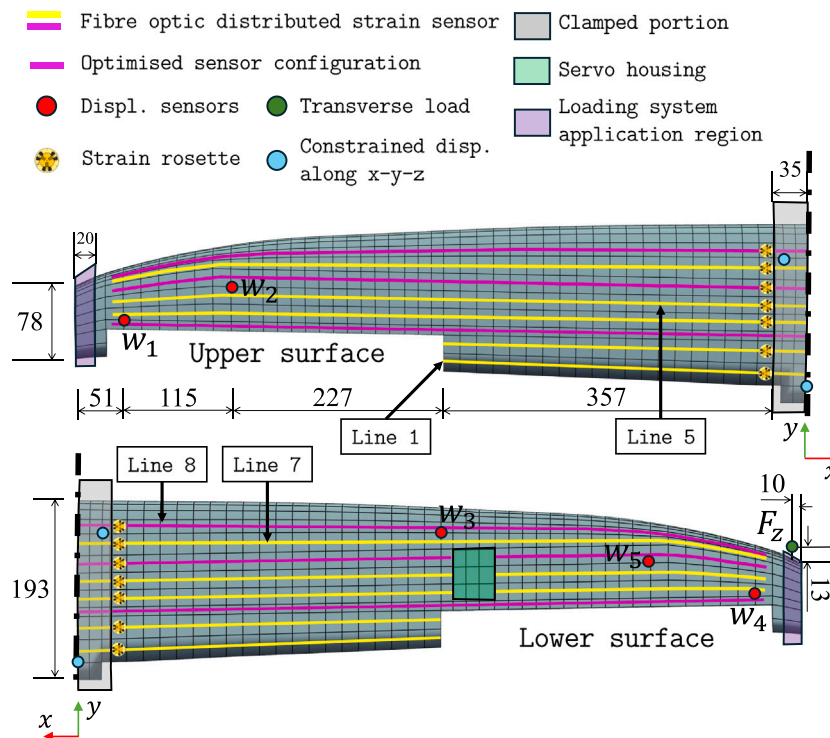


Fig. 10. iFEM mesh and sensor configuration — The figure shows the iFEM mesh, the applied load location, and the arrangement of both strain and displacement sensors. The installed fibre sensors define eight sensing lines on both top and bottom wing surfaces. These lines are represented by magenta and yellow. The subset of magenta lines correspond to the optimised sensor set described in Section 3.4. The labels of the strain sensing lines analysed in Section 3.4 are also included. All dimensions are expressed in mm.

strain information. This condition represents an interesting and realistic challenge for applying the shape-sensing process to real structures characterised by areas that are either difficult or impossible to reach. The SSB-iFEM perfectly adapts to this condition, since its formulation does not require sensors on both surfaces of a thin-walled structure. Moreover, SSB-iFEM is perfectly adaptable to conditions where it is the external surface to be inaccessible or to configurations with sensors on both sides at different locations, without compromising its validity. Therefore, its application to the test case is straightforward and requires no modification. On the contrary, the original iFEM requires a back-to-back sensor configuration to compute the experimental strain measures (membrane strains and bending curvatures) included in the error functional of Eq. (9). Therefore, applying iFEM to the current test case requires some hypotheses on the internal strains. If we consider the half-wing as a beam-like structure under bending deformation, the axial strains have a linear distribution along the thickness of the wing airfoil. If the thickness of the skin is smaller compared to the thickness of the airfoil, the variation of the strains along the skin's thickness can be considered negligible with respect to the total variation of the strains along the wing cross-section [34,52]. Therefore, a constant strain assumption can be made for the strains on the top and bottom surfaces of the wing's skin. Although this is a strong assumption when considering the actual behaviour of the test case, a more complex derivation of the internal strains, i.e. using extrapolation techniques, would increase the complexity of the process for the application of standard iFEM, thus leading to a non-equal comparison with the straightforward application of SSB-iFEM. When assuming a through-the-thickness constant strain for the original iFEM, the procedure will be defined as Constant Strain-iFEM (CS-iFEM).

The strain sensors are installed on the external surface of the half-wing according to the scheme in Fig. 10. A fifteen-meter-long distributed fibre optic strain sensor based on the Rayleigh back-scattering and Optical Frequency Domain Reflectometry (OFDR) [54] is attached to the wing's upper and lower surfaces so that eight sensing lines along

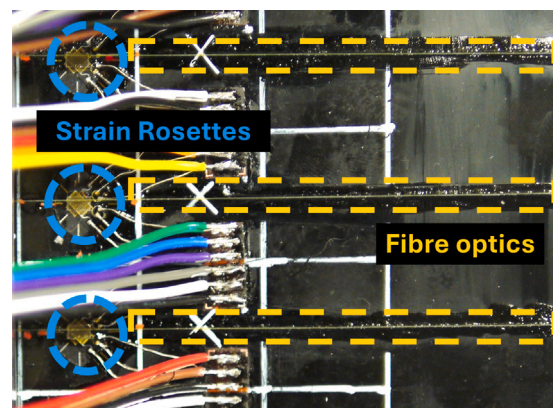


Fig. 11. Detail of the strain sensors installed at the root section of the wing.

the wingspan are obtained. On these lines, the high-density sensor is able to measure the strain along the fibre direction in every centroid of the inverse elements that lie underneath the sensor itself. Thanks to the presence of the silicone layers, the fibre is also installed in the portion of the half-wing clamped between the aluminium blocks, so that any eventual deformation in the clamped area can be measured. In addition, fourteen strain rosettes are installed in proximity to the root section of the wing (Fig. 10). These sensors can measure the strain along different directions than the axial direction available with the fibre. Seven of them are installed on the upper and seven on the lower surface of the half-wing. A detailed view of the installed strain sensors is presented in Fig. 11.

The experimental strain sensor configuration installed on the wing covers the majority of the elements of the inverse model, and it can feed the shape-sensing algorithm with an impressive amount of data. However, according to previous investigations, this amount is reasonably

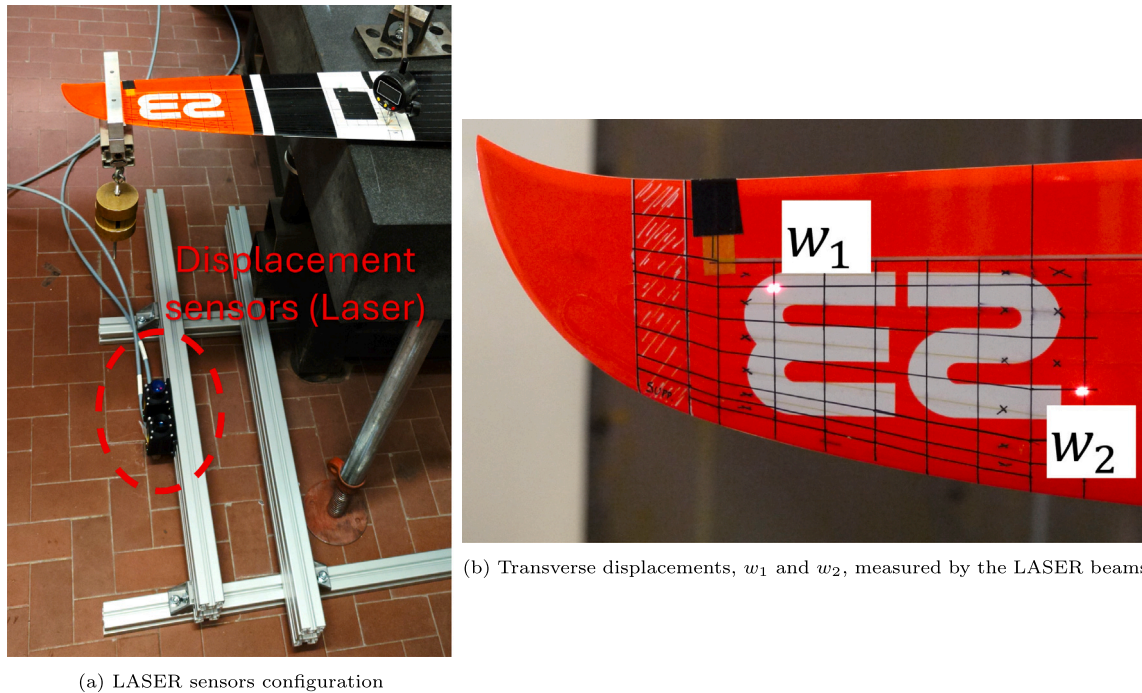


Fig. 12. LASER displacement sensors.

unnecessary for the iFEM, which can obtain accurate reconstructions of the displacement field with sparser sensor configurations. In standard iFEM and, more generally, in shape-sensing applications, the strain sensor configuration is usually selected through an Optimised Sensor Placement (OSP) procedure. However, these procedures require performing shape sensing with different sensor configurations to find the optimal one according to a defined selection process. This task can only be accomplished if the whole strain field of the structure is known, typically by analysing a high-fidelity structural model of the structure, which requires a priori detailed knowledge of the material mechanical characteristics. One of the novelties of the present work is related to this condition. The wing tested for this application is representative of a real-world scenario where a high-fidelity model cannot be designed because of the lack of sufficient information. Therefore, the wing is initially instrumented with a sensor configuration meant to cover almost the entire geometry of the structure. The optimisation of sensors is carried out after the first experimental strains are obtained in order to prove that a reduced and affordable number of sensors is sufficient to perform accurate shape sensing. The a-posteriori experimental optimisation will be described in Section 3.4.

Finally, to assess the accuracy of the displacement reconstruction, two transverse deflections (w_1 , w_2) of the wing are measured on the upper and one (w_3) on the lower surface of the half-wing. Two time-of-flight LASER sensors (optoNCDT ILR2250 by Micro-epsilon) are installed on the floor, as shown in picture 12(a), to measure the two deflections on the upper surface (Figs. 10 and 12(b)). On the other hand, one Linear Variable Transducer (LVDT) is installed on the lower surface to measure the w_3 transverse displacement, as illustrated in Fig. 7. The three reference displacements are broadly distributed over the structure's geometrical domain to evaluate the global accuracy of the shape sensing in different zones and surfaces.

3.4. Results

The experiment is performed by loading the clamped half-wing with increasing loads from 0 to 2.0 kg. During the test, the strains and the deflections w_1 , w_2 and w_3 are measured by the sensors. Simultaneously, the strain data are used to compute the whole displacement field

Table 1

Static test results for $F_z = 2.0$ kg and considering all the installed strain sensors.

	Exp. values [mm]	SSB-iFEM [mm]	ERR [%]	CS-iFEM [mm]	ERR [%]
w_1	18.34	18.15	-1.1	0.82	-2140.9
w_2	12.35	11.99	-2.9	2.32	-431.6
w_3	4.85	4.59	-5.4	1.42	-242.4

with SSB-iFEM and CS-iFEM. The nodal transverse displacements corresponding to the measured ones are extracted from the reconstructed deformed shape and compared to the sensor data.

The first analysis is performed considering the inputs from all the installed strain sensors. Due to the linearity observed in all the experimental data, only the results for the maximum load of 2.0 kg are reported in Table 1. The constant strain assumption is enforced by assigning the strain value measured by the sensors on the skin's external surface to the internal surface as well. The percentage errors in the reconstruction of the displacements, reported in Table 1, show a significant accuracy of the SSB-iFEM, with errors that do not exceed 5.4%. Moreover, the reconstruction of the maximum displacement (w_1) is impressively precise, showing an error of approximately 1%. On the contrary, the errors exhibited by CS-iFEM are significant, revealing a total misinterpretation of the deformed shape, since the maximum measured displacement is the smallest one in the reconstruction. These results prove that the constant strain hypothesis is incorrect for this structure. However, the need for the standard iFEM formulation of back-to-back sensors in a case like that, where the physical installation of sensors inside the wing is impossible, can only be satisfied with this kind of hypothesis or with a complex procedure that will make the method much less efficient than SSB-iFEM.

Once the superior accuracy of SSB-iFEM is assessed, the problem of having too many strain sensors on the structure can be addressed. An optimisation is performed by searching for a subset of sensors leading to a displacement field reconstruction as accurate as the one obtained with the full set. The standard sensor optimisation procedure is typically performed using data from a high-fidelity finite element

(FE) model of the structure and optimising the sensor configuration for various loading conditions. However, in this work, the objective is to demonstrate the accuracy and flexibility of the SSB-iFEM approach under conditions where only limited information about the structure is available and no high-fidelity model exists. Furthermore, one of the goals of the optimisation is to show that the method can operate effectively with a reduced number of sensors, regardless of how this configuration is obtained. Therefore, the optimisation is carried out using experimental data from the single loading condition of the static assessment. Previous studies have shown [42,55] that iFEM-based approaches exhibit good flexibility of the sensor configuration with respect to different loading conditions. Similarly, in this work, the adaptability of the experimentally-obtained optimised sensor configuration will be demonstrated under a different loading condition during the wind tunnel test, as discussed in Section 4.

The experimental optimisation procedure consists of defining a certain number of sensors and trying all the combinations of that number of sensors. In the context of this optimisation, one sensor is considered to be a single rosette or a single sensing line of the fibre (from root to tip). For example, to start, four sensors are selected: two lines of fibre and two strain rosettes. Therefore, all the existing combinations of two lines and two rosettes are tested with SSB-iFEM, and the errors on the measured displacements are computed. This procedure is performed for an increasing number of sensors, until the errors reach, with a satisfactory approximation, the one obtained with the full set of sensors. The identified minimum number of sensors that lead to accurate shape sensing is six. In particular, the use of six sensing lines, without any rosette, gives the errors summarised in Table 2. Fig. 10 shows the selected six strain sensing lines with magenta lines. The configuration includes three sensing lines on the upper surface of the wing and three corresponding lines on the lower surface. Therefore, this layout can be considered a globally back-to-back configuration, different from a standard back-to-back arrangement where the sensors are located on both sides of the thin-walled parts of the structure. The sensors' setup covers a broad area of the structure and guarantees extreme accuracy to the SSB-iFEM. On the contrary, using CS-iFEM with the optimised sensor configuration still leads to extremely inaccurate shape-sensing predictions. These results are demonstrated by the errors in Table 2 and the reconstructed deformed shape reported in Fig. 13. In particular, the deformed shape reconstructed with CS-iFEM (Fig. 13(b)) highlights the limitations of this formulation. The reconstructed deformation exhibits significant torsion, which is not present in the actual half-wing static response. The line of nodes where w_1 is measured corresponds to the torsion axis of this misinterpreted deformation, and along this line the deflection is nearly zero. A key limitation of the constant strain hypothesis is that the ratio between the skin thickness and the overall thickness of the half-wing varies along the chord. In the thicker region of the airfoil, the assumption of a negligible skin thickness compared to the overall section thickness is more realistic. However, while the skin thickness remains constant along the span, the airfoil thickness decreases towards the wing-tip. This causes the thickness ratio to vary along the span, implying that the constant strain assumption can only be reasonably enforced near the root section and where the airfoil is thicker. In fact, even in lines of nodes near the leading edge, CS-iFEM is able to reconstruct only a small portion of the actual bending of the structure. Conversely, moving closer to the trailing edge, the constant strain assumption becomes increasingly inaccurate. As a result, in that area, CS-iFEM completely fails to capture the bending of the half-wing, leading to zero transverse displacements. Once again, it is important to note that enforcing a different, more accurate assumption on the through-the-thickness distribution of strains in standard iFEM is extremely difficult, or even unfeasible, for such a complex structure. This clearly highlights a limitation compared to the straightforward application of SSB-iFEM, when sensors are available on one surface only.

Table 2

Static test results for $F_z = 2.0$ kg and considering the six sensing lines included in the optimised strain sensors configuration.

	Exp. values [mm]	SSB-iFEM [mm]	ERR [%]	CS-iFEM [mm]	ERR [%]
w_1	18.34	18.15	-1.1	1.69	-983.2
w_2	12.35	12.02	-2.7	2.90	-325.2
w_3	4.85	4.59	-5.6	1.35	-259.7

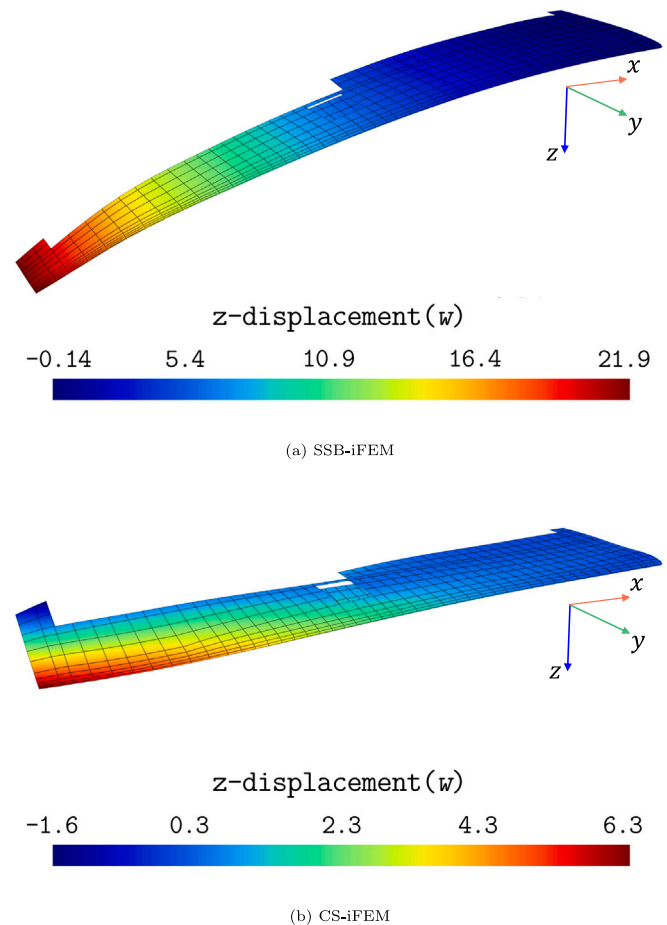


Fig. 13. Reconstructed deformed shape coloured with values of z -displacement (w) in mm. Results have been obtained with SSB-iFEM (a) and CS-iFEM (b) when the optimised sensor configuration is considered.

A further comparison is carried out to assess the ability of the SSB-iFEM to reconstruct the strain field accurately. Since the CS-iFEM fails to reconstruct the displacement field, no strain results obtained using this methodology will be discussed. Specifically, the experimental strain measurements are compared with the reconstructed values for the two sensor configurations presented earlier: the full sensor configuration (with sixteen sensing lines), and the optimised one (with six sensing lines shown in Fig. 10). The results of the strain reconstruction are evaluated for some lines on the upper and lower surfaces of the wing. Specifically, lines 7 and 8 for the lower surface, and lines 1 and 5 for the upper surface; their location is also shown in Fig. 10. The chosen lines are representative of the entire range of strain reconstruction behaviours observed, and the corresponding results are reported in Fig. 14. It is worth noting that, in the full sensor configuration, all the selected lines are also sensing lines, meaning that the strain data are used as input in SSB-iFEM reconstruction. Conversely, in the optimised sensor configuration, only line 8 among the selected ones is also a sensing line.

As expected, the SSB-iFEM is highly accurate in reconstructing strain distributions that have been used as input data for the inverse

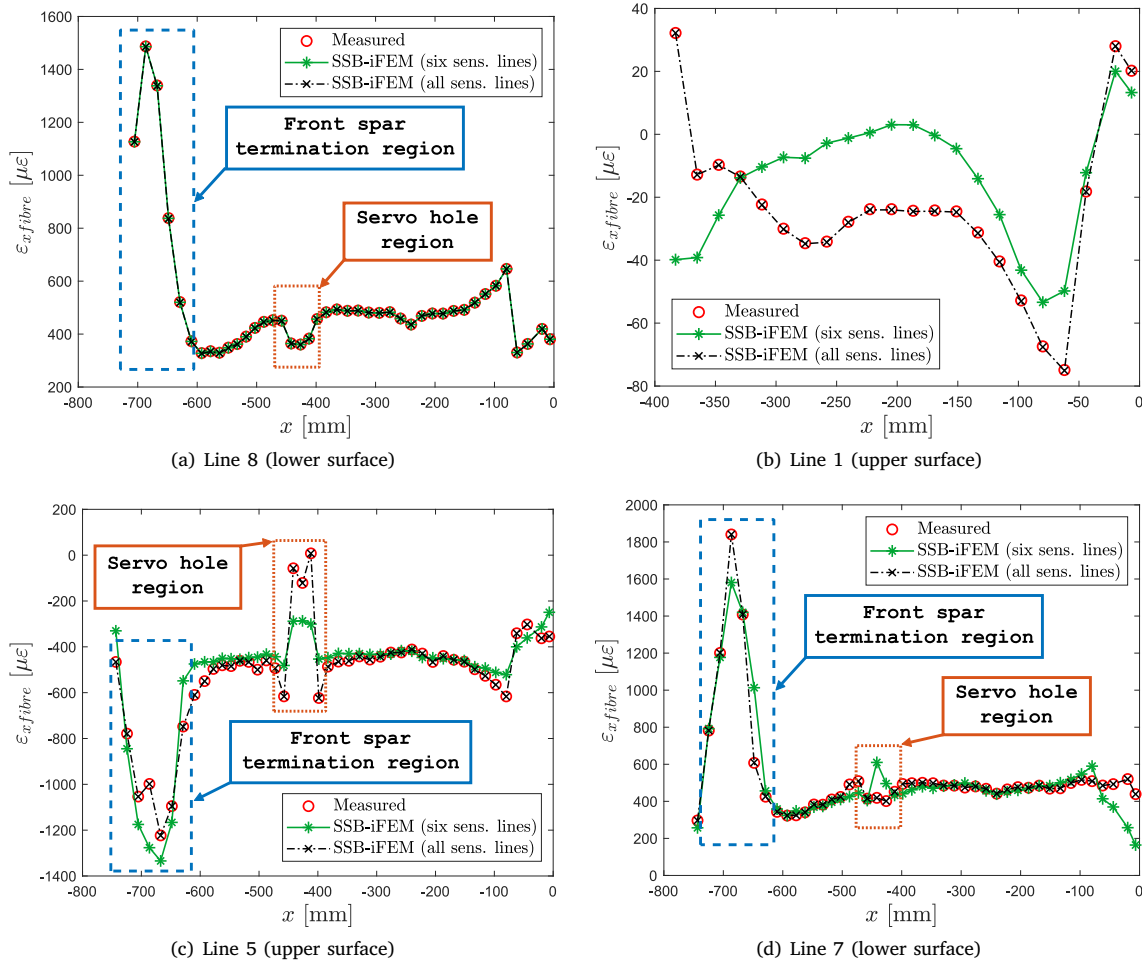


Fig. 14. Measured and reconstructed strain distributions using SSB-iFEM along four different lines (see Fig. 10 for reference) on the upper and lower surfaces. For each line, the SSB-iFEM strain reconstruction is obtained with the optimised sensor configuration (six sensing lines) and the full one (all sensing lines).

analysis. This happens for the considered lines when the full set of sensors is used to provide strain input data, Fig. 14, and is confirmed for line 8 when adopting the optimised set of sensors, since this set includes that line, Fig. 14(a). Conversely, some differences are observed when strain reconstruction is performed, where the strain input data have not been used. This is the case of the results for lines 1, 5, and 7 obtained with the optimised set of sensors. For example, as shown in Fig. 14(b), the reconstructed strain values in the optimised sensor configuration are very different from the measured ones, with errors that in some cases exceed 100%. However, it should be noted that the measured strains for line 1 are one order of magnitude lower than those in the other cases, and the values are very close to zero, which makes the discrepancies in the reconstruction for these points acceptable. Fewer discrepancies and lower errors are observed in the reconstructed strain distributions of Figs. 14(c) and 14(d) for lines 5 and 7. A further confirmation of the robustness and relative accuracy of the SSB-iFEM in reconstructing the strain field, even with a reduced number of sensors, is proven by its ability to reproduce with good fidelity some local strain effects of this wing structure, such as the peak strain values caused by the termination of the front spar or the strain redistribution associated by the presence of the servo hole, as highlighted in Figs. 14(a), 14(c) and 14(d). Although some errors remain in the reconstruction (see, for instance, lines 5 and 7 in Figs. 14(c) and 14(d)), the optimised configuration is still able to detect these local strain phenomena with a good degree of accuracy. Moreover, the overall performance is further assessed by computing the percentage

Root Mean Square Error (RMSE) between all the reconstructed and the measured strain data. Its definition follows:

$$RMSE_{\epsilon}(\%) = \sqrt{\frac{1}{N} \sum_{i=1}^N \left(\frac{\epsilon_i^m - \epsilon_i^{rec}}{\max(\epsilon^m)} \right)^2} \cdot 100 \quad (22)$$

where N is the total number of strain measurements included in the full set of sensors, ϵ_i^m is the i th measured strain value, and ϵ_i^{rec} is the corresponding i th reconstructed value. The RMSE values for the optimised and full sensor configurations are 3.47% and 0.0034%, respectively, both of which are considered reasonable for validating the strain field reconstruction.

4. Real-time wind tunnel test

In this section, an additional test is conducted to demonstrate the efficiency and accuracy of the SSB-iFEM. Specifically, two critical aspects of the technology are investigated: the ability to monitor a structure under operating dynamic conditions, and the capability to perform such a task in real time. These features are assessed through a wind tunnel test on the wing structure.

4.1. Testing configuration

The wing used in this experiment is the same as the one analysed during the static campaign (Section 3). It is installed in the 3-meter-diameter wind tunnel of the Modesto Panetti Aerodynamic Laboratory

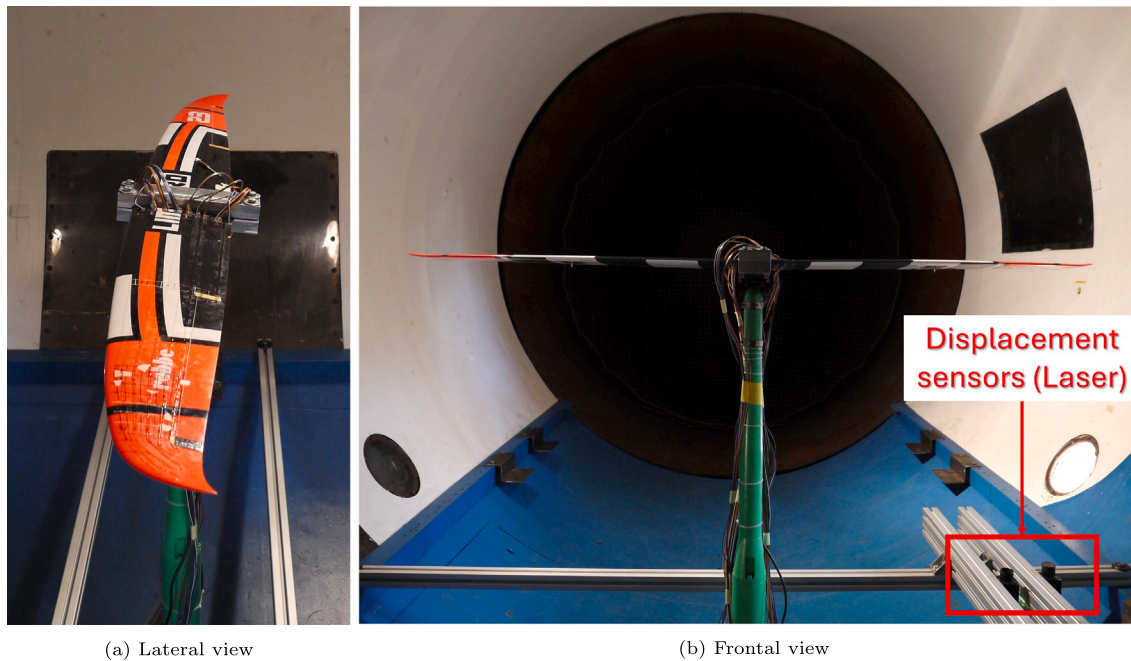


Fig. 15. Wind tunnel testing configuration.

at Politecnico di Torino. The wing is positioned at the centre of the test chamber and connected to the tunnel's post through the same aluminium plates adopted to simulate the fuselage–wing connection in the static test. An angle of attack of $+5^\circ$ is imposed. Unlike the previous test, the wing is mounted in a right-side-up configuration, so that the generated lift and the resulting deformation act in the standard upward direction. Fig. 15 show the wing mounted inside the tunnel. For this test as well, displacement sensors were required to validate the reconstructions obtained with SSB-iFEM.

Two time-of-flight LASER sensors (optoNCDT ILR2250 by Micro-epsilon), mounted on the base of the tunnel (Fig. 15(b)), are used to measure the wing deflection at two points on the lower surface, near the tip. The two points are shown in Fig. 10 with the labels w_4 and w_5 .

The strain sensor configuration installed on the structure is identical to that used in the static test, comprising the 15-meter-long fibre and the 14 strain rosettes. However, to evaluate under different loading conditions the robustness of the optimised sensor configuration derived from the static analysis, only the reduced set of six sensing lines defined in that configuration was considered in this test.

4.2. Real-time monitoring

The realisation of a real-time monitoring framework requires achieving extreme computational efficiency for the SSB-iFEM algorithm, as well as developing an effective communication protocol between the physical sensors and the digital inverse model. The SSB-iFEM algorithm is inherently efficient thanks to its formulation. The reconstruction of the displacements is obtained by solving the system of linear algebraic equations described by Eq. (21). The coefficient matrix, \mathbf{K}' , which must be inverted to solve the problem, depends on the sensor configuration through the penalisation factors λ and on the mesh of the monitored structure through the shape functions. Conversely, the vector of known terms, \mathbf{F}' , depends on the same inputs but also on the strain data acquired from the sensors. In a real-time monitoring context, where both the sensor configuration and the inverse model are fixed, the coefficient matrix \mathbf{K}' remains constant over time and therefore needs to be inverted only once. The vector \mathbf{F}' , on the other hand, must be continuously updated with new strain data from the sensors at each

time step. Nevertheless, updating this vector and multiplying it by the already inverted matrix \mathbf{K}' is a computationally inexpensive process, thus enabling fast and real-time computation of the displacement degrees of freedom (DOFs). Although it has been proven to be impractical for this application, it is important to note that the standard iFEM formulation shares the exact same characteristics as SSB-iFEM in terms of computational efficiency and real-time capabilities.

The second crucial component for real-time monitoring is the design of a fast communication protocol to transmit the sensor data to the digital model. The acquisition system for the distributed strain-sensing fibre is the Luna ODISI 6000 interrogator. This device enables real-time streaming of strain sensor data through a TCP/IP communication protocol. The strain measurements are transmitted as JSON streaming data packets.

In this application, the data transmission to the DIMOSS[®] software, where the SSB-iFEM digital model is elaborated, is achieved through a Wi-Fi network. This enhances the capability to monitor the structure not only in real time but also remotely. The real-time monitoring system operates by directly acquiring the data packets and processing them to continuously update the \mathbf{F}' vector with the new incoming data at each time step. Then, the computation of the displacement field is obtained through a simple vector–matrix multiplication, and the digital model is updated accordingly. The updating of the model is visualised in real time on the structure mesh in terms of the deformed shape and of the von Mises strain field. In Fig. 16, the real-time monitoring process is schematised.

4.3. Sensor data processing

The preliminary tests in the wind tunnel were performed by accelerating the airflow from 0 to 20 m/s and measuring the strains from the optical fibre. These tests highlighted an issue with the strain-sensing data. Although the variation in flow speed was kept gradual, the interaction between the flow and the structure induced vibrations in the latter. These vibrations resulted in disturbances in the strain signal, with the strain profile along the fibre length presenting several Not a Number (NaN) values for air speeds exceeding 16 m/s, as shown in Fig. 17(a). The figure reports the signal from a segment of the fibre

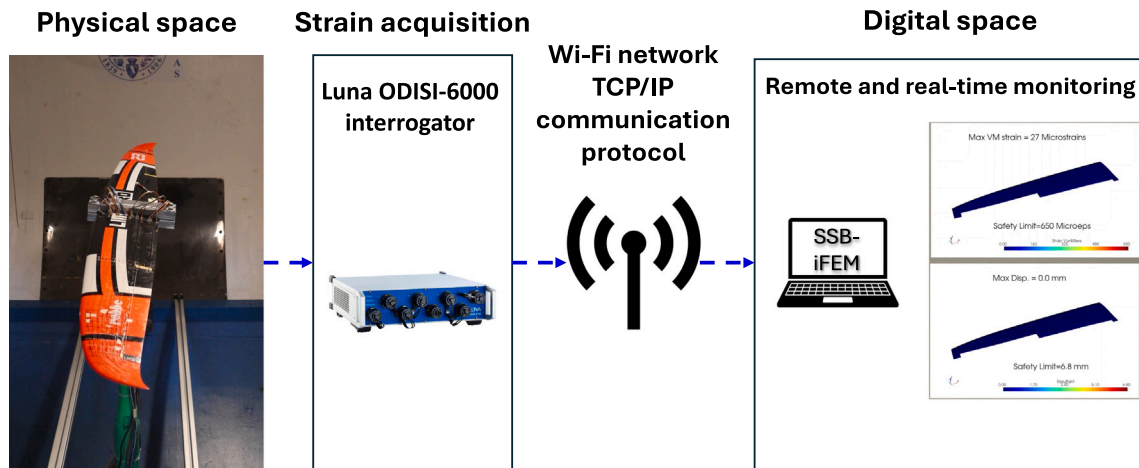


Fig. 16. Communication protocol and real-time monitoring workflow.

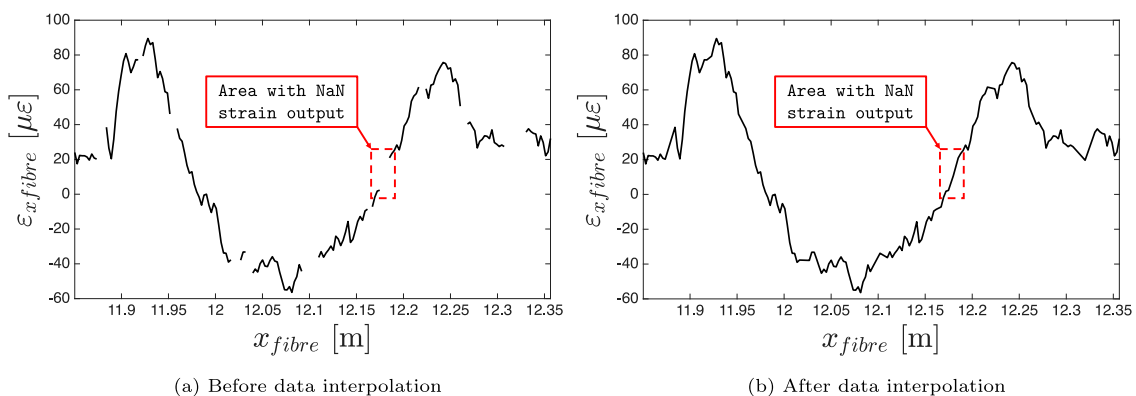


Fig. 17. Strain data vibration induced error. The figure shows the output from a segment of the strain measuring fibre. In (a), several areas where NaN values, induced by the vibration, are shown as missing strain values, and one of them is highlighted. In (b), the same segment is shown after spatial interpolation of the data has been performed.

immersed in an airflow at 18 m/s, where several points along the fibre length show missing data.

The distributed fibre optic strain sensor used in this application is based on Rayleigh backscattering and Optical Frequency Domain Reflectometry (OFDR). This system provides an impressive density of strain measurements along the fibre, with a measurement point every 2.6 mm. However, according to the manufacturer, Luna Innovations, the sensor can withstand a maximum dynamic loading rate of 5 Hz [56]. It is therefore highly probable that, for air speeds exceeding 16 m/s during the wind tunnel tests, the induced vibration frequency surpassed this limitation, resulting in local measurement failures. Nevertheless, the high spatial resolution of the sensor allowed for an effective and reliable data post-processing. The NaN values were replaced by performing a linear spatial interpolation of the valid data, as illustrated in Fig. 17(b). This post-processing step yielded clean strain data for air speeds up to 18 m/s. Moreover, the linear spatial interpolation is computationally inexpensive, allowing the monitoring to be performed in real time.

4.4. Results

The live monitoring was tested in the wind tunnel by accelerating the airflow from 0 to 18 m/s while simultaneously collecting strain data and performing shape sensing using the SSB-iFEM algorithm.

The streaming of the data and the consequent updating of the digital model are performed at a rate of 25 Hz. This frequency represents the limit of the fibre optic acquisition system and is not related to the computational speed of the SSB-iFEM real-time monitoring. The upper working limit of the algorithm could not be tested at higher rates due to this sensing limitation.

The first acceleration phase, from 0 m/s to 10 m/s, occurred rapidly over approximately 20 s, whereas the subsequent acceleration from 10 m/s to 18 m/s was performed gradually, with stops of 40–60 s at each 1 m/s increment. A video of one of the performed tests demonstrates the real-time monitoring process (<https://youtu.be/HbQsPRh0Xrc> or *Watch the video*). The video has been sped up to make the structural deformation more perceptible. As it can be observed, the reconstructed displacement is perfectly synchronised with the actual deformation, resulting in an excellent match between the physical structure and its digital twin. In the video, a warning message appears whenever a maximum displacement threshold of 7 mm is exceeded. This serves as an example of how the technology could be used to indicate, in real time, critical flight conditions. Fig. 18 shows the monitored wing at a specific time step during the test at 18 m/s.

Once the synchronisation of the monitoring is verified, its accuracy must be demonstrated. To this end, the reference displacement data from the laser sensors are compared with the displacements reconstructed at the same locations using SSB-iFEM. Fig. 19 shows the time

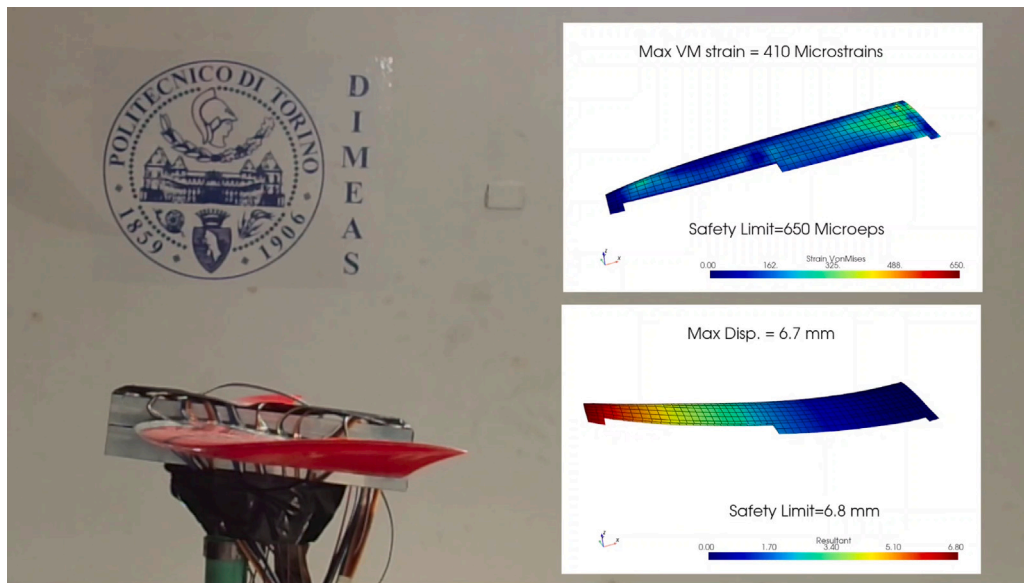


Fig. 18. Live monitoring of the wing deformation at 18 m/s air speed. A complete recording of the experiment is available at <https://youtu.be/HbQsPRh0Xrc> or Watch the video.

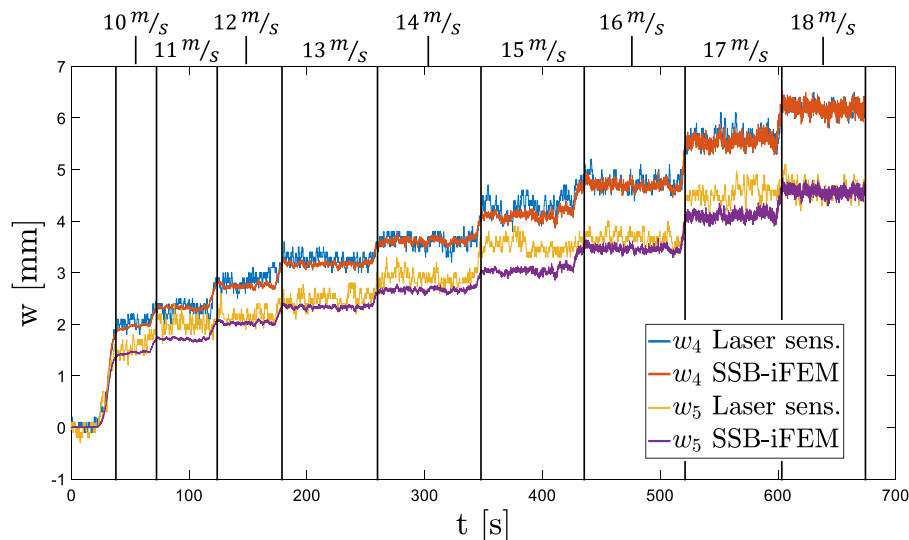


Fig. 19. Time history of the measured (Laser sens.) and reconstructed (SSB-iFEM) transverse displacements w_4 , w_5 for a varying airflow speed between 10–18 m/s.

histories of the measured reference displacements and the corresponding reconstructed values over an entire wind tunnel experiment. It is important to note that these displacements are measured at the w_4 and w_5 positions, which are not located at the tip of the wing model. Consequently, the maximum displacement observed in the video and in Fig. 18 is not reached at these points, which explains the difference in the measured values. The analysis of the graph shows a good agreement between the measured and reconstructed displacements, particularly for higher displacement values, where the signal-to-noise ratio is higher. The details of the maximum displacement condition of w_4 at the maximum speed of 18 m/s are presented in Fig. 20. The graph highlights that the SSB-iFEM reconstruction of the transverse displacement is highly accurate, successfully capturing even the small fluctuations in displacement induced by the wing's vibration. However, at lower air speeds, corresponding to reduced aerodynamic loads, particularly for w_5 , the reconstructions exhibit slight discrepancies.

To more rigorously evaluate the overall accuracy of the shape-sensing approach over the entire test, a statistical analysis of the

reconstruction errors is performed. The absolute value of the percentage error with respect to the measured displacements is computed for w_4 and w_5 at each time step. From the resulting error time histories, box-and-whisker plots are derived (Fig. 21). In particular, Fig. 21(a) presents the plots for all time steps corresponding to air speeds between 10 m/s and 18 m/s. The median error amounts to only 2.6% for w_4 and 7.8% for w_5 . For w_4 , 75% of the errors are below 4.7%, and 97% are below 9.8%, with outliers representing merely 3% of the dataset. For w_5 , 75% of the errors do not exceed 11.6%, while 99.6% are lower than 22.3%, indicating the presence of only a few outliers. Despite the occurrence of a few statistically rare error values exceeding 11.6% for w_5 , the overall results confirm the excellent performance of the proposed shape-sensing approach. The limited number of higher errors does not compromise the general accuracy or consistency of the reconstructions, which remain highly reliable across the entire range of aerodynamic loads.

In Fig. 21(b), the box-and-whisker plot of the reconstruction error corresponding to the time steps during which the air speed of 18 m/s is reached and maintained is presented. This condition represents the

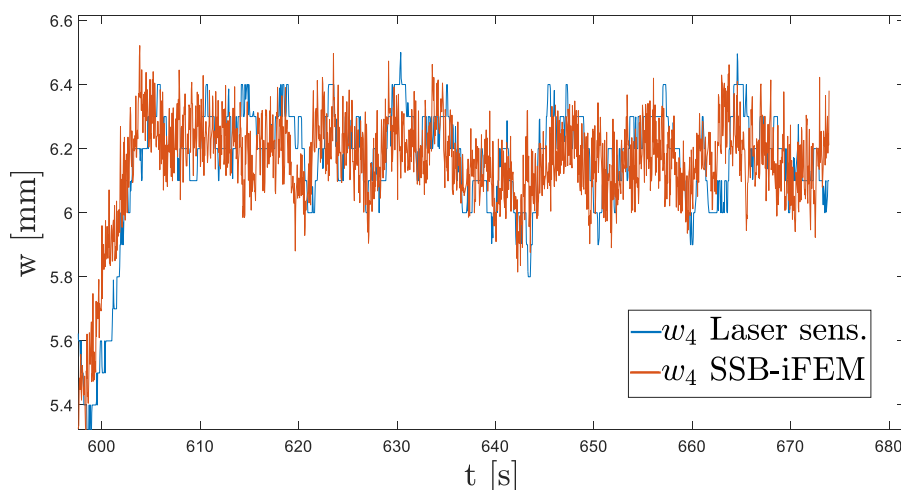


Fig. 20. Time history of the measured (Laser sens.) and reconstructed (SSB-iFEM) transverse displacements w_4 , for the maximum airflow speed of 18 m/s.

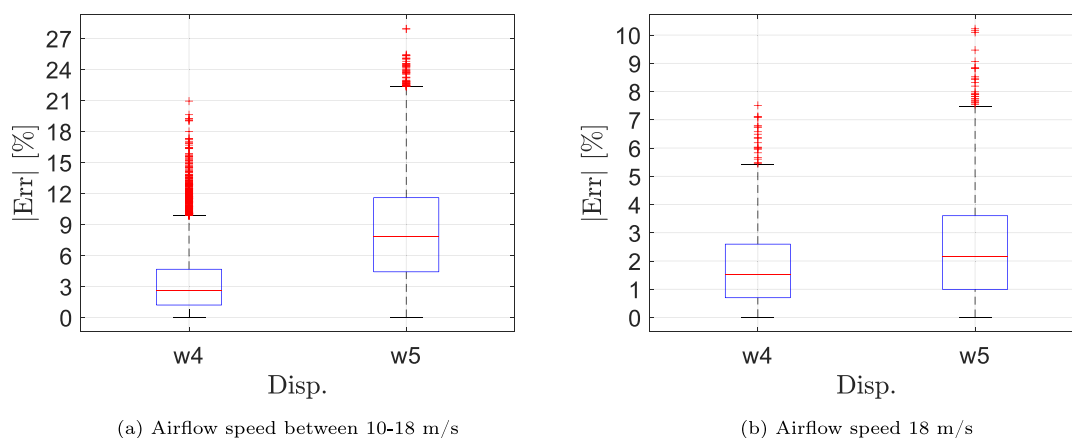


Fig. 21. Box and whiskers plot for the absolute value of the percentage error in the reconstruction of the w_4 and w_5 displacements.

most severe loading scenario, characterised by the largest structural displacements and the highest signal-to-noise ratio. Under these circumstances, the reconstruction results exhibit excellent accuracy. The median reconstruction errors for w_4 and w_5 are 1.5% and 2.1%, respectively. Furthermore, 98.6% of the w_4 errors are below 5.4%, and 75% of the data do not exceed a 2.6% error. The errors associated with the w_5 displacement are slightly higher, with 98% of the data below 7.5% and 75% of the errors below 3.6%. Even the outliers for both displacements do not exceed the 10.2% error value. These results demonstrate an even higher robustness and accuracy of SSB-iFEM in cases where the magnitude of the deformation leads to a high signal-to-noise ratio. The analysis of the errors under the highest deformation condition confirms the observations drawn from the analysis of Fig. 20. The SSB-iFEM demonstrates the capability to accurately reconstruct even small displacement fluctuations, exhibiting minimal reconstruction errors.

5. Conclusions

This study presents the first application of iFEM-based approaches to the experimental monitoring of the deformed shape of a real aerospace structure, both under static loading and in simulated operating conditions during a wind tunnel test. The analysed structure is

the half-wing of a commercial hotliner. The half-wing presents several characteristics that make it a challenging case for the application of standard shape-sensing techniques. Due to its commercial nature, only minimal information is available regarding its structural details. Consequently, a reverse engineering process is required to retrieve the essential data for monitoring purposes. In this context, the properties of iFEM-based techniques proved advantageous. These methods, which rely on the strain–displacement relationship, require only geometric information and do not depend on material properties. Furthermore, iFEM can reconstruct the displacement field of the entire structure even when certain components are not included in the digital model and their geometrical characteristics are unknown. In this case, for instance, the spars of the wing box were not included in either the reverse engineering process or in the monitoring model. An additional challenge arises from the impossibility of accessing the internal wing box for strain sensor installation. This limitation has historically hindered the application of standard iFEM techniques to such complex structures. The recent development of the SSB-iFEM formulation has addressed this issue. This novel approach is based on the direct computation of the error between the strains measured by sensors and their analytical counterparts, expressed as a function of unknown DOFs and known derivatives of the shape functions. As a result of this innovation, the

need for a back-to-back sensor configuration for each thin-walled part of the structure has been eliminated, thus making it possible to set strain sensors only on the external surface of the whole structure. Therefore, for this experimental activity, strain rosettes and distributed fibre optic strain sensors are installed on the external surface of the wing's skin only.

The experimental static assessment is conducted by statically applying a transverse load to the wing tip, while the root section of the structure is clamped. During the test, in addition to the strain data, deflections at three locations distributed across the structural domain are also measured to assess the accuracy of the shape-sensing approach. To evaluate the accuracy of SSB-iFEM, the method is benchmarked against the standard iFEM. However, applying iFEM with a sensor configuration limited to a single surface of a thin-walled structure requires the estimation of the missing strains on the opposite surface through specific assumptions. In this study, the typical strain field of a bending half-wing suggested the assumption of a through-the-thickness constant strain in the wing's skin. The experimental results show that SSB-iFEM accurately reconstructs the measured displacements, even when the number of strain sensors is reduced to only six sensing lines along the span of the structure. By contrast, the constant through-the-thickness strain assumption leads standard iFEM to an entirely incorrect deformation reconstruction. Therefore, this study demonstrates that SSB-iFEM effectively overcomes the limitation of back-to-back sensor configuration and significantly expands the applicability of iFEM-based approaches to real aerospace structures.

The dynamic wind tunnel test presented in this work represents the first experimental assessment of shape sensing for an aerospace structure under experimentally simulated operational conditions. The test is performed under the same sensor configurations as the static test. During the experiment, the airflow is accelerated up to 18 m/s, while the displacement and strain fields are reconstructed in real time using the SSB-iFEM approach and a continuous data exchange between the sensors of the real structure and its digital model, thus enabling the realisation of a true structural digital twin. The accurate results obtained in terms of displacement reconstruction demonstrate the applicability of SSB-iFEM for monitoring real aerospace structures in dynamic operational environments. However, the wind tunnel experiment also revealed a limitation of the sensing technology adopted for the test. The distributed fibre optic sensors based on Rayleigh backscattering and OFDR showed some limitations in capturing the dynamic phenomena induced by aerodynamic loads. The strain signal exhibited significant noise when the vibration level increased, particularly when the airspeed in the tunnel exceeded 16 m/s.

Although, in this work, the disturbances in the strain sensing signal were successfully mitigated through data filtering, future work should focus on improving the sensing technology from two perspectives. The first involves exploring alternative sensing technologies, such as fibre optic sensors based on Fibre Bragg Gratings (FBG) or traditional strain gauges. However, the adoption of these technologies leads to the second point of interest. Distributed fibre optic sensors based on Rayleigh backscattering and OFDR, despite their difficulties in dynamic conditions, provide an unmatched density of strain measurements compared to other technologies. Therefore, future studies should further investigate the capabilities of SSB-iFEM by assessing its potential not only for monitoring structures with single-sided sensor configurations but also for reducing sensor requirements, even in cases where both surfaces are accessible. Additionally, technologies capable of virtually expanding the information obtained from physical sensors should be explored.

CRediT authorship contribution statement

Marco Esposito: Writing – review & editing, Writing – original draft, Visualization, Validation, Supervision, Software, Resources,

Project administration, Methodology, Investigation, Funding acquisition, Formal analysis, Data curation, Conceptualization. **Matteo Sorrenti:** Writing – original draft, Visualization, Validation, Software, Methodology, Investigation, Formal analysis, Conceptualization, Data curation, Writing – review & editing. **Marco Gherlone:** Writing – review & editing, Writing – original draft, Supervision, Resources, Project administration, Methodology, Investigation, Conceptualization, Data curation, Formal analysis.

Declaration of competing interest

The authors declare the following financial interests/personal relationships which may be considered as potential competing interests: Marco Esposito reports financial support was provided by Compagnia di San Paolo. If there are other authors, they declare that they have no known competing financial interests or personal relationships that could have appeared to influence the work reported in this paper.

Acknowledgements

The authors gratefully acknowledge the Fondazione Compagnia di San Paolo for supporting this research activity by funding the DIMOSS project within the framework of the PoC Instrument 2022/2024, cut-off 3. The authors would like to thank the team of the Aeronautics Laboratory “Modesto Panetti” for their valuable support during the wind tunnel test campaign.

Appendix A. Matrices definition

The coefficient matrix \mathbf{K}^e and the vector \mathbf{f}^e , Eq. (14), can be computed as follows

$$\begin{aligned}\mathbf{K}^e &= \mathbf{K}_m^e + \mathbf{K}_k^e + \mathbf{K}_g^e \\ \mathbf{f}^e &= \mathbf{f}_m^e + \mathbf{f}_k^e + \mathbf{f}_g^e\end{aligned}\quad (\text{A.1})$$

where

$$\begin{aligned}\mathbf{K}_m^e &= \int_{A^e} [(\mathbf{B}^m)^T \text{diag}(\boldsymbol{\lambda}_m) \mathbf{B}^m] dA^e & \mathbf{f}_m^e &= \int_{A^e} [(\mathbf{B}^m)^T \text{diag}(\boldsymbol{\lambda}_m) \mathbf{m}^e] dA^e \\ \mathbf{K}_k^e &= (2t)^2 \int_{A^e} [(\mathbf{B}^k)^T \text{diag}(\boldsymbol{\lambda}_k) \mathbf{B}^k] dA^e & \mathbf{f}_k^e &= (2t)^2 \int_{A^e} [(\mathbf{B}^k)^T \text{diag}(\boldsymbol{\lambda}_k) \mathbf{k}^e] dA^e \\ \mathbf{K}_g^e &= \int_{A^e} [(\mathbf{B}^g)^T \text{diag}(\boldsymbol{\lambda}_g) \mathbf{B}^g] dA^e & \mathbf{f}_g^e &= \int_{A^e} [(\mathbf{B}^g)^T \text{diag}(\boldsymbol{\lambda}_g) \mathbf{g}^e] dA^e = \mathbf{0}\end{aligned}\quad (\text{A.2})$$

The coefficient matrix \mathbf{K}'^e and the vector \mathbf{f}'^e , Eq. (20), are defined as

$$\begin{aligned}\mathbf{K}'^e &= \mathbf{K}_p^{+e} + \mathbf{K}_p^{-e} + \mathbf{K}_g^e \\ \mathbf{f}'^e &= \mathbf{f}_p^{+e} + \mathbf{f}_p^{-e} + \mathbf{f}_g^e\end{aligned}\quad (\text{A.3})$$

where Eq. (A.4) is given in Box 1

with $\mathbf{Z}_{\varepsilon_p}^+ = \mathbf{Z}_{\varepsilon_p}(+t)$ and $\mathbf{Z}_{\varepsilon_p}^- = \mathbf{Z}_{\varepsilon_p}(-t)$.

Definitions (A.2) and (A.4) (and Eqs. (10), (11), (13), (17), (18) and (19) as well) are integrals over the element area although, in real applications, experimental measurements are defined in discrete locations. Refer to [34] for a complete discussion on how to efficiently compute these integrals.

Appendix B. Supplementary data

Supplementary material related to this article can be found online at <https://doi.org/10.1016/j.measurement.2026.120354>.

The video of the real-time monitoring during the wind tunnel test is available as supplementary material.

$$\begin{aligned}
 \mathbf{K}_p^{+e} &= \int_{A^e} \left[(\mathbf{B}^{mk})^T (\mathbf{Z}_{\varepsilon_p}^+)^T \text{diag}(\lambda_p^+) \mathbf{Z}_{\varepsilon_p}^+ \mathbf{B}^{mk} \right] dA^e & \mathbf{f}_p^{+e} &= \int_{A^e} \left[(\mathbf{B}^{mk})^T (\mathbf{Z}_{\varepsilon_p}^+)^T \text{diag}(\lambda_p^+) \boldsymbol{\varepsilon}_p^{\varepsilon+} \right] dA^e \\
 \mathbf{K}_p^{-e} &= \int_{A^e} \left[(\mathbf{B}^{mk})^T (\mathbf{Z}_{\varepsilon_p}^-)^T \text{diag}(\lambda_p^-) \mathbf{Z}_{\varepsilon_p}^- \mathbf{B}^{mk} \right] dA^e & \mathbf{f}_p^{-e} &= \int_{A^e} \left[(\mathbf{B}^{mk})^T (\mathbf{Z}_{\varepsilon_p}^-)^T \text{diag}(\lambda_p^-) \boldsymbol{\varepsilon}_p^{\varepsilon-} \right] dA^e
 \end{aligned} \tag{A.4}$$

Box I.

Data availability

Data will be made available on request.

References

- [1] C.R. Farrar, K. Worden, An introduction to structural health monitoring, *Philos. Trans. Royal Soc. A: Math. Phys. Eng. Sci.* 365 (1851) (2007) 303–315, <http://dx.doi.org/10.1098/rsta.2006.1928>.
- [2] M. Li, D. Jia, Z. Wu, S. Qiu, W. He, Structural damage identification using strain mode differences by the iFEM based on the convolutional neural network (CNN), *Mech. Syst. Signal Process.* 165 (2022) 108289, <http://dx.doi.org/10.1016/j.ymsp.2021.108289>.
- [3] F. Ganjdoust, A. Kefal, A. Tessler, Delamination detection and localization in vibrating composite plates and shells using the inverse finite element method, *Sensors* 23 (18) (2023) <http://dx.doi.org/10.3390/s23187926>.
- [4] R. Evenblij, F. Kong, C. Koimtzoglou, M. Ciminello, I. Dimino, A. Concilio, Shape sensing for morphing structures using fiber Bragg grating technology, in: P.C. Wolcken, M. Papadopoulos (Eds.), *Smart Intelligent Aircraft Structures*, SARISTU, Springer International Publishing, Cham, 2016, pp. 471–491, http://dx.doi.org/10.1007/978-3-319-22413-8_21.
- [5] V. Biscotti, R. Roy, M. Gherlone, Shape monitoring of morphing wing structures using the inverse finite element method, *Comput. Struct.* 309 (2025) 107652, <http://dx.doi.org/10.1016/j.compstruc.2025.107652>.
- [6] M. Gherlone, P. Cerracchio, M. Mattone, Shape sensing methods: Review and experimental comparison on a wing-shaped plate, *Prog. Aerosp. Sci.* 99 (April, 2018) 14–26, <http://dx.doi.org/10.1016/j.paerosci.2018.04.001>.
- [7] G. Foss, E. Haugse, Using modal test results to develop strain to displacement transformations, in: *Proceedings of the 13th International Modal Analysis Conference*, Nashville, 1995.
- [8] A.C. Pisoni, C. Santolini, D.E. Hauf, S. Dubowsky, Displacements in a vibrating body by strain gauge measurements, in: *Proceedings of the 13th International Modal Analysis Conference*, Nashville, 1995.
- [9] P. Bogert, E. Haugse, R. Gehrki, Structural shape identification from experimental strains using a modal transformation technique, in: *44th AIAA/ASME/ASCE/AHS/ASC Structures, Structural Dynamics, and Materials Conference*, Norfolk, 2003, <http://dx.doi.org/10.2514/6.2003-1626>.
- [10] S. Rapp, L.-H. Kang, J.-H. Han, U.C. Mueller, H. Baier, Displacement field estimation for a two-dimensional structure using fiber Bragg grating sensors, *Smart Mater. Struct.* 18 (2) (2009) 025006, <http://dx.doi.org/10.1088/0964-1726/18/2/025006>.
- [11] M. Freydin, M.K. Rattner, D.E. Raveh, I. Kressel, R. Davidi, M. Tur, Fiber-optics-based aeroelastic shape sensing, *AIAA J.* 57 (12) (2019) 5094–5103, <http://dx.doi.org/10.2514/1.J057944>.
- [12] W.L. Ko, W.L. Richards, V.T. Fleischer, Displacement Theories for In-Flight Deformed Shape Predictions of Aerospace Structures, Report NASA/TP-2007-214612, NASA Dryden Flight Research Center; Edwards, CA, United States, 2007, <https://ntrs.nasa.gov/citations/20070032936>.
- [13] W.L. Ko, W.L. Richards, V.T. Fleischer, Applications of the Ko Displacement Theory to the Deformed Shape Predictions of the Doubly-Tapered Ikhana Wing, Report NASA/TP-2009-214652, NASA Dryden Flight Research Center; Edwards, CA, United States, 2009, <https://ntrs.nasa.gov/citations/20090040594>.
- [14] C.V. Jutte, W.L. Ko, C.A. Stephens, J.A. Bakalyar, W.L. Richards, Deformed Shape Calculation of a Full-Scale Wing Using Fiber Optic Strain Data from a Ground Loads Test, Report NASA/TP-2011-215975, NASA Dryden Flight Research Center; Edwards, CA, United States, 2011, <https://ntrs.nasa.gov/citations/20120004140>.
- [15] Y. Yuan, W. Sun, Y. Zhang, P. Wang, S. Han, Research on error compensation methods of wing deflection reconstruction based on FBG strain sensors, *Aerosp. Sci. Technol.* 161 (2025) 110167, <http://dx.doi.org/10.1016/j.ast.2025.110167>.
- [16] C. Pak, Wing shape sensing from measured strain, *AIAA J.* 54 (3) (2016) 1068–1077, <http://dx.doi.org/10.2514/1.J053986>.
- [17] S.Z. Guoping Ding, W. Song, Strain - deformation reconstruction of CFRP laminates based on Ko displacement theory, *Nondestruct. Test. Eval.* 36 (2) (2021) 145–157, <http://dx.doi.org/10.1080/10589759.2019.1707200>.
- [18] J. Leng, K. Zuo, C. Xu, X. Zhou, S. Zheng, J. Kang, Q. Liu, X. Chen, W. Shen, L. Wang, R.X. Gao, Physics-informed machine learning in intelligent manufacturing: a review, *J. Intell. Manuf.* (2025) <http://dx.doi.org/10.1007/s10845-025-02641-1>.
- [19] S. Meyer zu Westerhausen, I. Hichri, K. Herrmann, R. Lachmayer, Optimisation of sensor and sensor node positions for shape sensing with a wireless sensor network—A case study using the modal method and a physics-informed neural network, *Sensors* 25 (17) (2025) <http://dx.doi.org/10.3390/s25175573>.
- [20] A. Tessler, J. Spangler, A least-squares variational method for full-field reconstruction of elastic deformations in shear-deformable plates and shells, *Comput. Methods Appl. Mech. Engrg.* 194 (2) (2005) 327–339, <http://dx.doi.org/10.1016/j.cma.2004.03.015>, Selected papers from the 11th Conference on The Mathematics of Finite Elements and Applications.
- [21] A. Kefal, E. Oterkus, A. Tessler, J.L. Spangler, A quadrilateral inverse-shell element with drilling degrees of freedom for shape sensing and structural health monitoring, *Eng. Sci. Technol. An Int. J.* 19 (3) (2016) 1299–1313, <http://dx.doi.org/10.1016/j.jestch.2016.03.006>.
- [22] A. Kefal, An efficient curved inverse-shell element for shape sensing and structural health monitoring of cylindrical marine structures, *Ocean Eng.* 188 (2019) 106262, <http://dx.doi.org/10.1016/j.oceaneng.2019.106262>.
- [23] A. Kefal, E. Oterkus, Isogeometric iFEM analysis of thin shell structures, *Sensors* 20 (9) (2020) <http://dx.doi.org/10.3390/s20092685>.
- [24] E. Del Priore, L. Lampani, A methodology for applying isogeometric inverse finite element method to the shape sensing of stiffened thin-shell structures, *Thin-Walled Struct.* 199 (2024) 111837, <http://dx.doi.org/10.1016/j.tws.2024.111837>.
- [25] A. Tessler, R. Roy, M. Esposito, C. Surace, M. Gherlone, Shape sensing of plate and shell structures undergoing large displacements using the inverse finite element method, *Shock Vib.* 2018 (1) (2018) 8076085, <http://dx.doi.org/10.1155/2018/8076085>.
- [26] M. Li, D. Jia, H. Huang, Geometrically nonlinear deformation reconstruction based on iQS4 elements using a linearized iterative iFEM algorithm, *Acta Mech. Solida Sin.* 36 (2023) 166–180, <http://dx.doi.org/10.1007/s10038-022-00369-6>.
- [27] P. Cerracchio, M. Gherlone, M. Di Sciuva, A. Tessler, A novel approach for displacement and stress monitoring of sandwich structures based on the inverse finite element method, *Compos. Struct.* 127 (2015) 69–76, <http://dx.doi.org/10.1016/j.compstruct.2015.02.081>.
- [28] A. Kefal, A. Tessler, E. Oterkus, An enhanced inverse finite element method for displacement and stress monitoring of multilayered composite and sandwich structures, *Compos. Struct.* 179 (2017) 514–540, <http://dx.doi.org/10.1016/j.compstruct.2017.07.078>.
- [29] F. Zhao, H. Bao, J. Liu, K. Li, Shape sensing of multilayered composite and sandwich beams based on refined zigzag theory and inverse finite element method, *Compos. Struct.* 261 (2021) 113321, <http://dx.doi.org/10.1016/j.compstruct.2020.113321>.
- [30] M. Gherlone, P. Cerracchio, M. Mattone, M. Di Sciuva, A. Tessler, Shape sensing of 3D frame structures using an inverse finite element method, *Int. J. Solids Struct.* 49 (22) (2012) 3100–3112, <http://dx.doi.org/10.1016/j.ijsolstr.2012.06.009>.
- [31] F. Zhao, L. Xu, H. Bao, J. Du, Shape sensing of variable cross-section beam using the inverse finite element method and isogeometric analysis, *Measurement* 158 (2020) 107656, <http://dx.doi.org/10.1016/j.measurement.2020.107656>.
- [32] R. Roy, M. Gherlone, C. Surace, A shape sensing methodology for beams with generic cross-sections: Application to airfoil beams, *Aerosp. Sci. Technol.* 110 (2021) 106484, <http://dx.doi.org/10.1016/j.ast.2020.106484>.
- [33] M. Esposito, R. Roy, C. Surace, M. Gherlone, Hybrid shell-beam inverse finite element method for the shape sensing of stiffened thin-walled structures: Formulation and experimental validation on a composite wing-shaped panel, *Sensors* 23 (13) (2023) <http://dx.doi.org/10.3390/s23135962>.
- [34] M. Esposito, M. Gherlone, Composite wing box deformed-shape reconstruction based on measured strains: Optimization and comparison of existing approaches, *Aerosp. Sci. Technol.* 99 (2020) 105758, <http://dx.doi.org/10.1016/j.ast.2020.105758>.
- [35] M. Esposito, M. Gherlone, Material and strain sensing uncertainties quantification for the shape sensing of a composite wing box, *Mech. Syst. Signal Process.* 160 (2021) 107875, <http://dx.doi.org/10.1016/j.ymsp.2021.107875>.
- [36] F. Valoriani, M. Esposito, M. Gherlone, Shape sensing for an UAV composite half-wing: Numerical comparison between modal method and Ko's displacement theory, *Aerospace* 9 (9) (2022) <https://www.mdpi.com/2226-4310/9/9/509>.

- [37] Z. Zhao, K. Chen, Y. Liu, H. Bao, A large-scale sensor layout optimization algorithm for improving the accuracy of inverse finite element method, *Sensors* 23 (19) (2023) <http://dx.doi.org/10.3390/s23198176>.
- [38] A. Tessler, H. Riggs, C.E. Freese, G.M. Cook, An improved variational method for finite element stress recovery and a posteriori error estimation, *Comput. Methods Appl. Mech. Engrg.* 155 (1) (1998) 15–30, [http://dx.doi.org/10.1016/S0045-7825\(97\)00135-7](http://dx.doi.org/10.1016/S0045-7825(97)00135-7).
- [39] A. Kefal, I.E. Tabrizi, M. Yildiz, A. Tessler, A smoothed iFEM approach for efficient shape-sensing applications: Numerical and experimental validation on composite structures, *Mech. Syst. Signal Process.* 152 (2021) 107486, <http://dx.doi.org/10.1016/j.ymssp.2020.107486>.
- [40] D. Oboe, L. Colombo, C. Sbarufatti, M. Giglio, Comparison of strain pre-extrapolation techniques for shape and strain sensing by iFEM of a composite plate subjected to compression buckling, *Compos. Struct.* 262 (2021) 113587, <http://dx.doi.org/10.1016/j.compstruct.2021.113587>.
- [41] R. Roy, M. Esposito, C. Surace, M. Gherlone, A. Tessler, Shape sensing of stiffened plates using inverse FEM aided by virtual strain measurements, in: P. Rizzo, A. Milazzo (Eds.), *European Workshop on Structural Health Monitoring*, Springer International Publishing, Cham, 2023, pp. 454–463, http://dx.doi.org/10.1007/978-3-031-07254-3_46.
- [42] M. Esposito, A novel shape sensing approach based on the coupling of modal virtual sensor expansion and iFEM: Numerical and experimental assessment on composite stiffened structures, *Comput. Struct.* 305 (2024) 107520, <http://dx.doi.org/10.1016/j.compstruc.2024.107520>.
- [43] A. Kefal, E. Oterkus, Displacement and stress monitoring of a Panamax containership using inverse finite element method, *Ocean Eng.* 119 (2016) 16–29, <http://dx.doi.org/10.1016/j.oceaneng.2016.04.025>.
- [44] A. Kefal, E. Oterkus, Displacement and stress monitoring of a chemical tanker based on inverse finite element method, *Ocean Eng.* 112 (2016) 33–46, <http://dx.doi.org/10.1016/j.oceaneng.2015.11.032>.
- [45] J. Bardiani, C. Oppezzo, A. Manes, C. Sbarufatti, An inverse FEM for structural health monitoring of a containership: Sensor network optimization for accurate displacement, strain, and internal force reconstruction, *Sensors* 25 (1) (2025) <http://dx.doi.org/10.3390/s25010276>.
- [46] J. Wang, L. Ren, R. You, T. Jiang, Z. Jia, G. xin Wang, Experimental study of pipeline deformation monitoring using the inverse finite element method based on the iBeam3 element, *Measurement* 184 (2021) 109881, <http://dx.doi.org/10.1016/j.measurement.2021.109881>.
- [47] P. Savino, F. Tondolo, Two-node curved inverse finite element formulations based on exact strain-displacement solution, *J. Appl. Comput. Mech.* 9 (1) (2023) 259–273, <http://dx.doi.org/10.22055/jacm.2022.41150.3708>.
- [48] D. Oboe, L. Colombo, C. Sbarufatti, M. Giglio, Shape sensing of a complex aeronautical structure with inverse finite element method, *Sensors* 21 (4) (2021) <http://dx.doi.org/10.3390/s21041388>.
- [49] M. Esposito, M. Mattone, M. Gherlone, Experimental shape sensing and load identification on a stiffened panel: A comparative study, *Sensors* 22 (3) (2022) <http://dx.doi.org/10.3390/s22031064>.
- [50] E.J. Miller, R. Manalo, A. Tessler, Full-Field Reconstruction of Structural Deformations and Loads from Measured Strain Data on a Wing Using the Inverse Finite Element Method, NASA/TM-2016-219407, 2016, <https://ntrs.nasa.gov/citations/20160014695>.
- [51] T. Huang, S. Yuan, J. Chen, T. Dong, W. Duan, Thermal deformation monitoring of large-scale composite honeycomb spaceborne antennas with limited strain measurements, *Aerosp. Sci. Technol.* 155 (2024) 109665, <http://dx.doi.org/10.1016/j.ast.2024.109665>.
- [52] V. Biscotti, M. Esposito, M. Gherlone, A new single sensor based iFEM formulation for shape-sensing of thin-walled structures instrumented with single-sided sensor configurations: Formulation, numerical assessment, and experimental validation, *Mech. Syst. Signal Process.* 232 (2025) 112700, <http://dx.doi.org/10.1016/j.ymssp.2025.112700>.
- [53] M. Esposito, M. Sorrenti, R. Roy, C. Surace, M. Gherlone, DIMOSS, a novel structural shape and stress monitoring software: Theoretical background and applications review, in: V. Lopresto, I. Papa (Eds.), *Dynamic Response and Failure of Composite Materials*, Springer Nature Switzerland, Cham, 2025, pp. 220–232, http://dx.doi.org/10.1007/978-3-031-77697-7_25.
- [54] B.J. Soller, D.K. Gifford, M.S. Wolfe, M.E. Froggatt, High resolution optical frequency domain reflectometry for characterization of components and assemblies, *Opt. Express* 13 (2) (2005) 666–674, <http://dx.doi.org/10.1364/OPEX.13.000666>.
- [55] M. Esposito, R. Roy, M. Gherlone, C. Surace, Structural deformation reconstruction using the hybrid shell-beam inverse finite element method: experimental application on a thin-walled stiffened panel, in: *COMPdyn 2023 - 9th ECCOMAS Thematic Conference on Computational Methods in Structural Dynamics and Earthquake Engineering*, ECCOMAS, 2023, <http://dx.doi.org/10.7712/120123.10648.20653>, ECCOMAS.
- [56] Luna Innovations, Luna odisi 6000 data sheet, 2022, <https://lunainc.com/sites/default/files/assets/files/data-sheet/Luna%20ODISI%206000%20Data%20Sheet.pdf>, (Accessed 17 November 2025).